Geochemistry Geophysics Geosystems G3
AN ELECTRONIC JOURNAL OF THE EARTH SCIENCES
Published by AGU and the Geochemical Society

Article
Volume 6, Number 7
7 July 2005
Q07001, doi:10.1029/2004GC000905
ISSN: 1525-2027

Modeling the effects of tidal loading on mid-ocean ridge hydrothermal systems

Timothy J. Crone and William S. D. Wilcock

School of Oceanography, University of Washington, Box 357940, Seattle, Washington 98195-7940, USA (tjc@ocean.washington.edu)

[1] Tidal signals are observed in numerous time-series measurements obtained from mid-ocean ridge hydrothermal systems. In some instances these tidal signals are clearly the result of ocean currents, but in other instances it appears that the signals may originate in the subseafloor formation. In order to explore the effect of ocean tidal loading on mid-ocean ridge hydrothermal systems, we apply a one-dimensional analytical model of tidal loading on a poroelastic half-space and develop a two-dimensional numerical model of tidal loading on a poroelastic convection cell. The one-dimensional models show that for a reasonable range of fluid, elastic, and hydrological properties, the loading efficiency may vary from near zero to near unity and the diffusive penetration depth for tidal pressure signals may vary from tens of meters to kilometers. The two-dimensional models demonstrate that tides may generate significant vertical and horizontal pressure gradients in mid-ocean ridge hydrothermal systems as a result of spatial variations in fluid temperatures and the elastic and hydrological properties of the crust. These continuum models predict that outflow temperature perturbations will be very small ($<10^{-4}$°C), but in real systems where the continuum hypothesis does not always apply, the perturbations may be on the order of $\sim$0.1°C. The models predict relatively large perturbations to fluid velocity at the seafloor. For high-temperature vents the outflow perturbations normalized to the mean flow velocity increase as the permeability decreases. Flow reversals at the seafloor are predicted in some regions of net low-temperature outflow and net inflow during the tidal cycle. In the subseafloor, tidally induced flow perturbations are likely to significantly enhance mixing and fluid exchange below the seafloor in regions of slow flow and in regions where there are strong gradients in temperature or in the mechanical and hydrological properties of the crust. Tidally enhanced mixing and fluid exchange may significantly influence the extent and character of microbial production in the subseafloor.

Components: 12,515 words, 16 figures, 6 tables.

Keywords: hydrothermal convection; modeling; poroelasticity; tidal loading.

Index Terms: 3021 Marine Geology and Geophysics: Marine hydrogeology; 3035 Marine Geology and Geophysics: Midocean ridge processes; 3045 Marine Geology and Geophysics: Seafloor morphology, geology, and geophysics.

Received 21 December 2004; **Revised** 20 March 2005; **Accepted** 27 April 2005; **Published** 7 July 2005.

Crone, T. J., and W. S. D. Wilcock (2005), Modeling the effects of tidal loading on mid-ocean ridge hydrothermal systems, *Geochem. Geophys. Geosyst.*, *6*, Q07001, doi:10.1029/2004GC000905.

1. Introduction

[2] Over the last two decades numerous studies have documented temporal variability in mid-ocean ridge hydrothermal systems by measuring a variety of properties, including temperature, velocity, heat flux, pressure, and resistivity [e.g., *Chevaldonné et al.*, 1991; *Converse et al.*, 1984; *Copley et al.*, 1999; *Fujioka et al.*, 1997; *Hutnak et al.*, 1999; *Johnson et al.*, 1994, 2000; *Jupp*, 2000; *Kadko*, 1994; *Kinoshita et al.*, 1996, 1998; *Larson and Lilley*, 2002; *Little et al.*, 1988; *McDuff and*

Delaney, 1995; *Pruis and Johnson*, 2004; *Sato et al.*, 1995; *Schultz et al.*, 1992, 1996; *Tivey et al.*, 2002]. In many of these studies the measured signals show modulations at tidal frequencies, fueling speculation that tidal loading interacts strongly with the hydrogeological system.

[3] In some instances, the tidally modulated signals can be attributed to tidally forced bottom currents. For example, the temperature measurements of *Chevaldonné et al.* [1991] were collected with temperature probes placed directly on the seafloor, and were almost certainly affected by currents. The temperature measurements of *Tivey et al.* [2002] contained spectral power at inertial frequencies, which strongly suggests an influence by tidal currents.

[4] In other instances, however, the signals are not obviously caused by bottom currents. For example, *Pruis and Johnson* [2004] obtained flow and temperature measurements with a device that was hydrologically sealed to the seafloor, and observed small variations in both properties that occurred approximately on tidal timescales. *Larson and Lilley* [2002] measured tidal variations in temperature and salinity with a device that was inserted well into the conduit of several black smokers, and was probably well-insulated from the effects of tidal currents. For such studies, there is a reasonable possibility that the tidally modulated signals are at least partially related to a subseafloor hydrological response to tidal loading.

[5] An obvious first step toward determining whether some tidal signals originate from beneath the seafloor is to generate models that can predict the effect of tidal loading on the underlying hydrothermal system. Such models would allow us to assess the possible magnitude of seafloor signals resulting from a subseafloor response to tidal loading, and thus assess whether past measurements might contain signals generated by those processes. Additionally, such models might lead to insights that could guide future field programs.

[6] A model of the hydrological response to tidal loading must include the effects of poroelasticity. The theory of poroelasticity describes the time-dependent response of a fluid-filled elastic porous medium to changes in stresses, and to pressure gradient anomalies [*Wang*, 2000]. In oceanic crust, changes in the overlying water height lead to both instantaneous and time-dependent changes in fluid pressure below the seafloor. An instantaneous pressure change occurs because a portion of any incremental change in seafloor load is instantaneously supported by the pore fluid pressure, while the remainder is supported by the frame of the porous medium. In a one-dimensional system, the parameter describing this partitioning of stress between the fluid and the frame is the loading efficiency. Subsequent to an instantaneous pressure change, a time-dependent pressure change will occur as fluid is forced to flow. This component of the pressure change is dependent upon the formation's permeability, the fluid viscosity, and the storage capacity of the system, which is a measure of the amount of fluid that must enter or leave the system to affect a given amount of pressure change. For periodic loading at the seafloor, this process is characterized by a length scale termed the penetration depth [*Wang and Davis*, 1996].

[7] In this paper, we use two types of poroelastic models to explore the hydrological response of mid-ocean ridge hydrothermal systems to tidal loading. We use a one-dimensional analytical model to predict the magnitude and character of pressure changes below the seafloor. We tie this model's input parameters to the seismic properties of the crust, and use it to predict the possible range of magnitudes for the instantaneous pressure response, and the possible range of length scales associated with the diffusive pressure response. From this model we infer that tidal loading may lead to significant perturbations in both vertical and horizontal pressure gradients in the ocean crust. To understand this process further, we develop a two-dimensional numerical model of poroelastic convection and use it to explore the effect of ocean tidal loading on the pressure, temperature, fluid velocity, and mechanical mixing within the upper part of a hydrothermal convection cell containing spatial variations in the elastic properties and permeability.

2. One-Dimensional Model

2.1. Equation Set

[8] The equation governing the change in pore pressure within a saturated porous semi-infinite half-space as a function of time t and depth z, subject to variable loading, is given by *van der Kamp and Gale* [1983], based on the theory of *Biot* [1941]:

$$\frac{\partial^2 p'}{\partial z^2} = \frac{1}{\eta}\left(\frac{\partial p'}{\partial t} - \gamma\frac{\partial \sigma_B}{\partial t}\right), \tag{1}$$

where

$$\eta = \frac{k}{\mu S}. \tag{2}$$

Wang and Davis [1996] develop a similar equation for a multiple-layered formation. The quantity p' is the change in fluid pressure (i.e., the departure from some reference pressure). The quantities γ and η are the loading efficiency and the hydraulic diffusivity, respectively; μ is the fluid viscosity, k is the formation permeability and σ_B is the ocean tidal loading function, with compressional stress being positive. The quantity S is the uniaxial storage compressibility, defined as

$$S = \left(\frac{1}{K} - \frac{1}{K_s}\right)\left(1 - \frac{4\psi}{3}\right) + \phi\left(\frac{1}{K_f} - \frac{1}{K_s}\right), \tag{3}$$

where K is the drained frame bulk modulus, K_s is the solid grain (rock) bulk modulus, K_f is the fluid bulk modulus, and ϕ is the porosity of the medium. Physically, S describes the amount of fluid that must be added or removed from an incremental volume of the porous medium to affect a given amount of pressure change while holding the material in a state of zero lateral strain. The dimensionless variable ψ is the poroelastic stress coefficient [*Detournay and Cheng*, 1993], defined as

$$\psi = \frac{\alpha(1 - 2\nu)}{2(1 - \nu)}, \tag{4}$$

where ν is the drained Poisson's ratio, and α is the Biot-Willis parameter:

$$\alpha = 1 - \frac{K}{K_s}. \tag{5}$$

The loading efficiency is defined as

$$\gamma = \frac{B(1 + \nu)}{3(1 - \nu) - 2\alpha B(1 - 2\nu)}, \tag{6}$$

where B is Skempton's coefficient, defined as

$$B = \alpha\left[\alpha + \phi K\left(\frac{1}{K_f} - \frac{1}{K_s}\right)\right]^{-1}. \tag{7}$$

[9] The loading efficiency and Skempton's coefficient are similar in that they both describe the change in pore pressure resulting from a change in externally applied compressive stress, with the loading efficiency being more applicable to one-dimensional systems.

[10] *Wang and Davis* [1996] rewrite equation (1) in terms of the instantaneous pressure change component p'_i and the diffusive pressure change component p'_d, which emphasizes the role γ and η play in characterizing the solution:

$$\frac{\partial p'_d}{\partial t} = \eta \frac{\partial^2 p'_d}{\partial z^2}, \tag{8}$$

$$p'_i = \gamma \sigma_B, \tag{9}$$

where

$$p' = p'_i + p'_d. \tag{10}$$

2.2. Analytical Solution

[11] An analytical solution to equation (1) is known for single-layer systems [*Fang et al.*, 1993], and multiple-layer systems [*Wang and Davis*, 1996]. If the ocean tidal loading function takes the form

$$\sigma_B(t) = \sigma_b \cos(2\pi f t), \tag{11}$$

then the solution for a single layer can be written::

$$p'(t, z) = \sigma_b \left\{ (1 - \gamma) e^{-\pi\left(\frac{z}{D_\zeta}\right)} \cdot \cos\left[2\pi f t - \pi\left(\frac{z}{D_\zeta}\right)\right] + \gamma \cos(2\pi f t) \right\}, \tag{12}$$

where

$$D_\zeta = \sqrt{\frac{\pi\eta}{f}}. \tag{13}$$

[12] The first term in equation (12) describes the diffusive component of the pore pressure change, which has an amplitude that decreases exponentially with depth and a phase lag relative to the loading function that increases linearly with depth. The quantity D_ζ is the penetration depth. At this depth the maximum amplitude of the diffusive component of p' has decreased to $\sigma_b(1 - \gamma)e^{-\pi}$. The second term in equation (12) describes the instantaneous component of the pore pressure change, which has an amplitude equal to γ times σ_b, is independent of depth, and is always in phase with the loading function.

2.3. Gassmann's Equation

[13] We use Gassmann's equation to obtain the drained parameters K and ν from crustal seismic properties. In its original form, Gassmann's equa-

Table 1. Baseline Input Parameters

Parameter[a]	Layer 2A	Layer 2B/C
	Solid (Rock) Properties	
c_s, J kg^{-1} K^{-1}	1004[b]	1004[b]
K_s, GPa	50[c]	70[d]
ρ_s, kg m^{-3}	2950[e]	2950[e]
	Formation Properties	
k, m^2	10^{-13}	10^{-14}
V_P, m s^{-1}	2400[f]	5500[g]
ν_u	0.48[h]	0.30[i]
ϕ	0.20[j]	0.03[k]
	Other Parameters	
f, s^{-1}	$1/45 \times 10^{-3}$[l]	$1/45 \times 10^{-3}$[l]
$\mathbf{g}$, m s^{-2}	9.8	9.8
p, Pa	22×10^6	22×10^6
T, °C	0	0
λ_s, W m^{-1} K^{-1}	2[e]	2[e]
σ_b, Pa	10^4[m]	10^4[m]

[a] See Notation section for symbol descriptions.
[b] *Touloukian et al.* [1981].
[c] *Christensen and Salisbury* [1972].
[d] *Pros et al.* [1962].
[e] *Turcotte and Schubert* [1982].
[f] *Carlson* [1998].
[g] *Vera et al.* [1990].
[h] *Christeson et al.* [1994].
[i] *Shaw* [1994].
[j] *Luyendyk* [1984].
[k] *Becker* [1985].
[l] Tidal loading frequency corresponds to a 12.5-hour tidal period.
[m] Tidal loading amplitude corresponds to a ~1 m tide.

tion relates the undrained bulk modulus of a porous medium to its drained bulk modulus, constituent bulk moduli, and porosity [*Gassmann*, 1951]:

$$K_u = K_s \frac{K + Q}{K_s + Q}, \tag{14}$$

where

$$Q = \frac{K_f (K_s - K)}{\phi (K_s - K_f)}. \tag{15}$$

By rearranging this equation and applying some basic relationships between the elastic moduli and seismic velocities, *Murphy et al.* [1991] give the velocity form of Gassmann's equation:

$$\left(\frac{V_P}{V_S}\right)^2 = \frac{\left(1 - \frac{K}{K_s}\right)^2}{G\left(\frac{\phi}{K_f} + \frac{1-\phi}{K_s} - \frac{K}{K_s^2}\right)} + \frac{K}{G} + \frac{4}{3}. \tag{16}$$

We express the shear modulus G in terms of the bulk density ρ and the S wave velocity V_S:

$$G = \rho V_S^2, \tag{17}$$

where

$$\rho = \rho_f \phi + \rho_s (1 - \phi), \tag{18}$$

and solve for K to obtain what we call the velocity-density form of Gassmann's equation:

$$K = \frac{\rho V_S^2 \left[\frac{4}{3} - \left(\frac{V_P}{V_S}\right)^2\right] \left[\frac{\phi}{K_f} + \frac{(1-\phi)}{K_s}\right] + 1}{\frac{\rho V_S^2}{K_s^2} \left[\frac{4}{3} - \left(\frac{V_P}{V_S}\right)^2\right] - \left[\frac{\phi}{K_f} - \frac{(1+\phi)}{K_s}\right]}. \tag{19}$$

It should be noted that the shear modulus G is the same for the drained and undrained conditions if we assume that the medium is isotropic and that the shear stress makes no contribution to fluid pressure. In this study we use ν_u and V_P to specify V_S, where

$$V_S = V_P \sqrt{\frac{1 - 2\nu_u}{2 - 2\nu_u}}. \tag{20}$$

To obtain K for use in our models, we choose a base temperature and pressure to obtain K_f and ρ_f from the equation of state. We choose values for K_s, ρ_s, ϕ, V_P, and ν_u for use in equations (18)–(20), and obtain ν with

$$\nu = \frac{3K - 2G}{2(3K + G)}. \tag{21}$$

The values we use to compute K are found in Tables 1 and 2.

Table 2. Baseline Derived Parameters

Parameter[a]	Layer 2A	Layer 2B/C
	Fluid Properties[b]	
c_f, J kg^{-1} K^{-1}	3962	3962
K_f, GPa	2.07	2.07
μ, Pa s	1.79×10^{-3}	1.79×10^{-3}
ρ_f, kg m^{-3}	1043	1043
	Other Derived Parameters	
V_S, m s^{-1}	471	2940
ρ, kg m^{-3}	2569	2893
G, GPa	0.57	25.0
K, GPa	7.4	49.5
K_u, GPa	14.0	54.2
λ, GPa	7.06	32.8
ν	0.46	0.28
α	0.85	0.29
ψ	0.059	0.089
B	0.55	0.30
S, Pa^{-1}	1.98×10^{-10}	1.93×10^{-11}
S_ϵ, Pa^{-1}	1.10×10^{-10}	1.83×10^{-11}
γ	0.52	0.18
η, m^2 s^{-1}	0.28	0.29
D_ζ, m	199	202

[a] See Notation section for symbol descriptions.
[b] Computed from the equations of state described in the text.

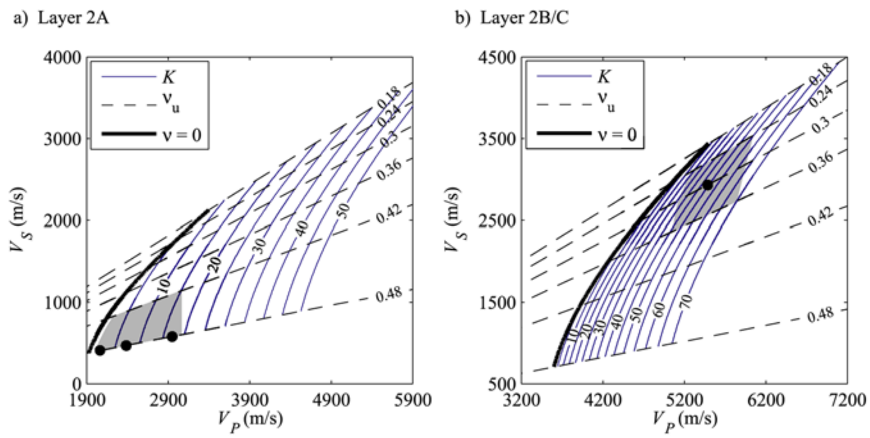

Figure 1. Solution of the velocity-density form of Gassmann's equation (19) for (a) typical layer 2A properties and (b) typical layer 2B/C properties (Tables 1 and 2). Solid contours depict the drained frame bulk modulus K in GPa; dashed contours depict the undrained Poisson's ratio ν_u. The solution in both panels is bounded at the top of the domain by $\nu_u = 0.18$ and at the bottom of the domain by $\nu_u = 0.48$. The solution is bounded on the right by the grain bulk modulus: 50 GPa in Figure 1a and 70 GPa in Figure 1b, since the drained frame bulk modulus cannot exceed this value. The solution is bounded on the left by the thick curve, corresponding to $\nu = 0$. Shaded regions within each panel correspond to typically measured seismic properties for each seismic layer. The solid black circles in each panel show the values of K used in the two-dimensional models discussed later in this paper. At lower porosities the P wave velocity becomes less dependent upon the drained frame bulk modulus. Also, it is interesting to note that Gassmann's equation predicts a minimum and maximum P wave velocity for a given porosity, Poisson's ratio, fluid and frame bulk modulus, and bulk density.

2.4. Input Parameters

[14] The input and derived parameters used in this study are listed in Tables 1 and 2, respectively. For the formation seismic properties and porosity we use typical values reported in the literature for younger sections of oceanic crustal layers 2A and 2B/C. In some of our results we explore a range of seismic properties. For the rock properties of layer 2A we use values reported for unfractured basalt. For the rock properties of layer 2B/C, we use values reported for diabase when available, otherwise we use values for basalt. We use an equation of state [*Holzbecher*, 1998] for pure water to determine the viscosity of the pore fluid as a function of temperature. We use a combination of two equations of state [*Anderko and Pitzer*, 1993; *Pitzer et al.*, 1984] for 3.2 wt% NaCl-H_2O solution to determine the density and bulk modulus of the pore fluid as a function of temperature and pressure.

[15] The permeability of oceanic crust can vary by many orders of magnitude, and is strongly anisotropic, heterogeneous, and scale-dependent [*Fisher*, 1998]. Furthermore, there are no direct measurements of permeability in zero-age crust. Hydrothermal convection models have been used to infer permeabilities indirectly, and typically yield values in the range 10^{-13} m^2 to 10^{-12} m^2 [e.g., *Cherkaoui et al.*, 1997; *Lowell and Germanovich*, 1994; *Wilcock and McNabb*, 1996; *Wilcock and Fisher*, 2004]. However, these estimates are depth-integrated values that average the permeability down to the base of the hydrothermal system. The permeability of layer 2A is likely to be much higher; off-axis studies suggest that layer 2A permeabilities may be as high as 10^{-9} m^2 at large length scales [*Davis et al.*, 2000]. Within sedimented sections of the mid-ocean ridge, the permeability can be very low, with 10^{-17} m^2 being a typical value [e.g., *Fisher et al.*, 1994]. Because permeabilities are so poorly constrained, we explore a large range, from 10^{-17} m^2 to 10^{-9} m^2.

2.5. One-Dimensional Results

[16] Figure 1 shows solutions to the velocity-density form of Gassmann's equation (19) for typical layer 2A and 2B/C properties. The drained frame bulk modulus K is strongly influenced by P wave velocity V_P, and increases with increasing V_P. K is more weakly influenced by S wave velocity V_S, and decreases with increasing V_S. In layer 2B/C, K is a stronger function of V_P than in layer 2A, as a result of the lower porosity in the lower layer.

[17] Gassmann's equation suggests that in layer 2A, where P wave velocities are low and Poisson's ratio is high, K is likely to be on the same order as

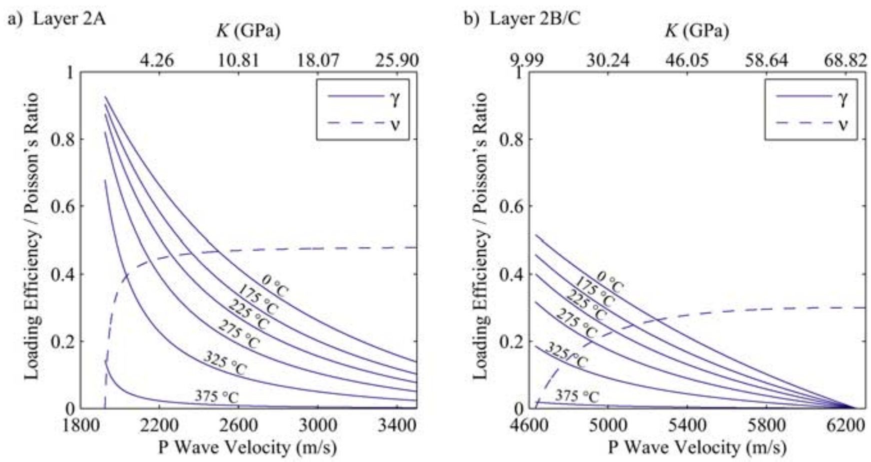

Figure 2. Solution of the loading efficiency equation (6) as a function of P wave velocity for (a) typical layer 2A properties and (b) typical layer 2B/C properties (Tables 1 and 2). Solid contours show the loading efficiency γ for six different interstitial fluid temperatures. The dashed curve shows the drained Poisson's ratio predicted by Gassmann's equation (19). The top axis shows the drained frame bulk modulus K (note that this scale is nonlinear). The curves are truncated on the left when the predicted drained Poisson's ratio falls below zero. In Figure 2b the curves are truncated on the right when the drained frame bulk modulus required to support higher P wave velocities becomes larger than the grain bulk modulus; this condition leads to nonphysical (negative) loading efficiencies. Loading efficiencies near mid-ocean ridge hydrothermal upflow zones may range from nearly zero to nearly unity as a result of highly variable fluid temperatures and elastic properties.

K_f for cold seawater, and range from about 0–5 GPa. This inference is consistent with the findings of *Davis et al.* [2000], who used borehole measurements to infer a drained bulk modulus of 3 GPa for layer 2A at two sites approximately 25 and 35 km from the spreading axis of the Juan de Fuca Ridge. In layer 2B/C, where P wave velocities are higher and Poisson's ratio is lower, K is likely to be on the same order as K_s, and range from about 50–70 GPa.

[18] Figure 2 shows solutions to the loading efficiency equation (6) for typical layer 2A and 2B/C properties and a range of fluid temperatures. Above 50°C, increases in temperature result in lowered loading efficiencies as a result of decreased fluid bulk modulus. Though it cannot be seen in this figure, the bulk modulus of seawater increases over the range 0–50°C, which drives the loading efficiency up slightly over this temperature range. In layer 2A (Figure 2a), where the drained frame bulk modulus is on the same order as the fluid bulk modulus, the loading efficiency can vary from near zero to near unity. Cold fluid within a compliant frame leads to the highest loading efficiencies, while hot fluid within a stiff frame leads to the lowest loading efficiencies. In layer 2B/C (Figure 2b) there is a similar dependence of loading efficiency upon fluid temperature, but because K is higher, the highest loading efficiencies are about 0.5.

[19] Figure 3 shows the penetration depth of diffusive pore pressure changes as a function of permeability and pore fluid temperature for a 12.5-hour tide and typical layer 2A and 2B/C properties. The permeability is the primary control on penetration, with penetration depths increasing as the square root of the permeability. This result is easily predicted from the form of equation (13). The mechanical properties of the formation frame exert a secondary control, with the increased bulk modulus and decreased porosity in layer 2B/C (Figure 3b) serving to increase the penetration depth compared to layer 2A (Figure 3a). This occurs because the storage capacity of the formation decreases with increasing stiffness and decreasing porosity, and thus less fluid must diffuse to affect a given pressure change. The mechanical and transport properties of the fluid also exert a secondary control on the penetration depth. The fluid viscosity decreases with increasing temperature, leading to an increase in penetration depth with fluid temperature. The fluid's bulk modulus decreases with temperature, leading to an increase in storage capacity and a decrease in penetration depth with fluid temperature. These two competing effects lead to a penetration depth maximum

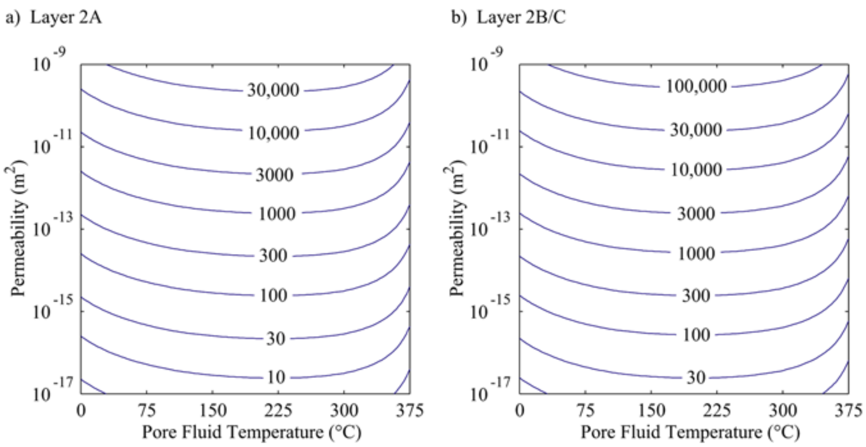

Figure 3. Contours of diffusive penetration depth D_ζ for a semidiurnal tide as a function of pore fluid temperature and permeability for (a) typical layer 2A properties and (b) typical layer 2B/C properties (Tables 1 and 2). The penetration depth is controlled primarily by the formation permeability. Fluid temperature exerts a secondary effect, with penetration depths reaching a maximum near 240°C and 200°C in Figures 3a and 3b, respectively, due to the competing effects of the fluid viscosity and fluid bulk modulus (see text). For a given permeability the penetration depth in layer 2B/C is predicted to be larger primarily because the increased drained frame bulk modulus leads to a lower storage capacity.

near 240 and 200°C for layer 2A and 2B/C, respectively.

[20] The results from these one-dimensional models suggest that relatively strong pressure gradients might be generated locally within mid-ocean ridge hydrothermal systems as a result of spatially varying fluid temperature, and spatially varying mechanical and hydrological properties of the formation. To gain a more quantitative insight into this possibility, we develop a two-dimensional finite-volume model of poroelastic convection. With this model we explore the effects of heterogeneity within the crust that arises from spatially varying fluid temperature, seismic properties, and permeability. We also explore some of the differences between these two-dimensional models and the one-dimensional theory.

3. Two-Dimensional Models

3.1. Equation Set

[21] The equations governing poroelasticity in two dimensions for the case of plane strain are derived in detail by *Wang* [2000]. Here we present a slightly modified form which allows for nonuniform elastic properties. There are four equations accounting for four dependent variables: horizontal displacement in the x direction u, vertical displacement in the z direction w, pore pressure p, and temperature T. The two mechanical equilibrium equations which account for displacement are

$$\frac{\partial}{\partial x}\left[\lambda\left(\frac{\partial u}{\partial x}+\frac{\partial w}{\partial z}\right)+2G\left(\frac{\partial u}{\partial x}\right)\right] + \frac{\partial}{\partial z}\left[G\left(\frac{\partial w}{\partial x}+\frac{\partial u}{\partial z}\right)\right] = \frac{\partial}{\partial x}\left[\alpha(p-p_0)\right], \quad (22)$$

and

$$\frac{\partial}{\partial z}\left[\lambda\left(\frac{\partial u}{\partial x}+\frac{\partial w}{\partial z}\right)+2G\left(\frac{\partial w}{\partial z}\right)\right] + \frac{\partial}{\partial x}\left[G\left(\frac{\partial w}{\partial x}+\frac{\partial u}{\partial z}\right)\right] = \frac{\partial}{\partial z}\left[\alpha(p-p_0)\right], \quad (23)$$

where λ is the drained Lamé parameter, p is the in situ pore pressure and p_0 is a reference pressure corresponding to zero strain. The fluid diffusion equation which accounts for pressure change is

$$S_\epsilon \frac{\partial p}{\partial t} + \nabla\cdot\boldsymbol{q} = -\alpha\frac{\partial}{\partial t}\left[\frac{\partial u}{\partial x}+\frac{\partial w}{\partial z}\right], \quad (24)$$

where S_ϵ is the constrained storage compressibility given by

$$S_\epsilon = \frac{\alpha^2}{K_u - K}, \quad (25)$$

and $\boldsymbol{q}$ is the Darcy velocity given by

$$\boldsymbol{q} = -\frac{k}{\mu}\left(\nabla p - \rho_f \boldsymbol{g}\right). \quad (26)$$

Bold-faced characters indicate vector quantities. Physically, S_ϵ describes the amount of fluid that must be added or removed from an incremental volume of the porous medium to affect a given amount of pressure change while holding the volume of the material constant. The equation for heat transport in a porous medium [*Turcotte and Schubert*, 1982] which accounts for temperature change is

$$\left((1-\phi)\rho_s c_s + \phi\rho_f c_f\right)\frac{\partial T}{\partial t} + \left(\rho_f c_f\right)\boldsymbol{q}\cdot\nabla T - \lambda_s\left(\nabla^2 T\right) = 0, \tag{27}$$

where c_s is the grain specific heat capacity, ρ_s is the grain density, c_f is the fluid specific heat capacity, ρ_f is the fluid density, and λ_s is the thermal conductivity of the fluid-solid mixture.

3.2. Numerical Solution

[22] We have developed a finite-volume code to obtain numerical solutions to equations (22)–(27) under a variety of conditions. We use a control volume approach [*Patankar*, 1980] for all spatial derivatives except those in the advective term of the heat equation, for which we use an upwind scheme. For these equations, this approach leads naturally to a staggered-grid system in which temperature and pressure are solved at control volume centers, and the Darcy velocity and displacements are solved at control volume faces. The staggered-grid, which is commonly used in numerical treatments of heat transfer and fluid flow [*Patankar*, 1980], eliminates the possibility of "checkerboard" instabilities that can arise when all quantities are solved at the same locations.

[23] We integrate equations (24) and (27) in time using a single-step implicit formulation. We estimate the strain-rate term in equation (24) using an explicit Euler formula in conjunction with the solution of equations (22) and (23) at the beginning and end of each time step. We then iterate over each time step to solve equations (24) and (27) simultaneously using a damped predictor-corrector scheme. The amount of damping applied to the displacements during the predictor-corrector loop is a function of the degree to which the mechanical equilibrium equations are coupled to the fluid diffusion equation. Stiffer frames reduce coupling, and damping can be accordingly reduced. We found empirically that a damping coefficient of $(1 - \gamma_{max})$, where γ_{max} is the maximum loading efficiency within the domain, provides optimal damping for rapid convergence. Benchmarks for our code are presented in Appendix A.

3.3. Models

[24] In order to illustrate the poroelastic response of the upper portion of a hydrothermal system to tidal loading and the effects of varying the elastic properties and the permeability, we present the results of seven models. Figure 4 shows the geometry and boundary conditions for these models. For each model, we solved equations (22)–(27) in a 600-m-deep by 1000-m-wide domain that represents a vertical cross section of the uppermost oceanic crust (i.e., seismic layer 2A) near a hydrothermal upflow zone. The shaded region is the nominal upflow zone which in some models is assigned a different permeability or P wave velocity than the surrounding formation. We refer to the area outside the upflow zone as the recharge zone. The numerical grid is a 75×125 array of 8-m-square finite-volume cells. Our second poroelastic benchmark (Table A2) suggests that this grid spacing is sufficient for permeabilities down to $\sim 10^{-14}$ m^2. The boundary conditions are the same for each model. The side boundaries are axes of symmetry; they are closed to fluid and heat flow, have zero displacements in the x direction, and sustain no shear stresses. The top boundary is open to fluid at seafloor pressures (mean pressure of 22 MPa), with a sinusoidal semidiurnal pressure variation of amplitude 10 kPa. The top boundary is closed to conductive heat transfer, but heat can cross the boundary by advection. Shear stress is zero on the top boundary. Hot hydrothermal fluid is forced into the model domain with a cold hydrostatic pressure gradient along a 120-m section of the bottom boundary adjacent to the left-hand side boundary. The rest of the bottom boundary is closed to heat and fluid flow. The inset graphs of Figure 4 show the temperature of fluid forced into the model, and the corresponding pressure gradient driving flow. The maximum fluid inflow temperature is 375°C. The entire bottom boundary has zero displacements in the z direction, and sustains no shear stresses.

[25] We have confirmed by conducting solutions with models of different dimensions that the conditions applied to the right and bottom boundaries have little effect on the solutions in the areas of interest for the solutions we present. The zero conductive heat flux condition on the top and bottom boundaries is a simplification that leads to near zero background temperatures in most of the

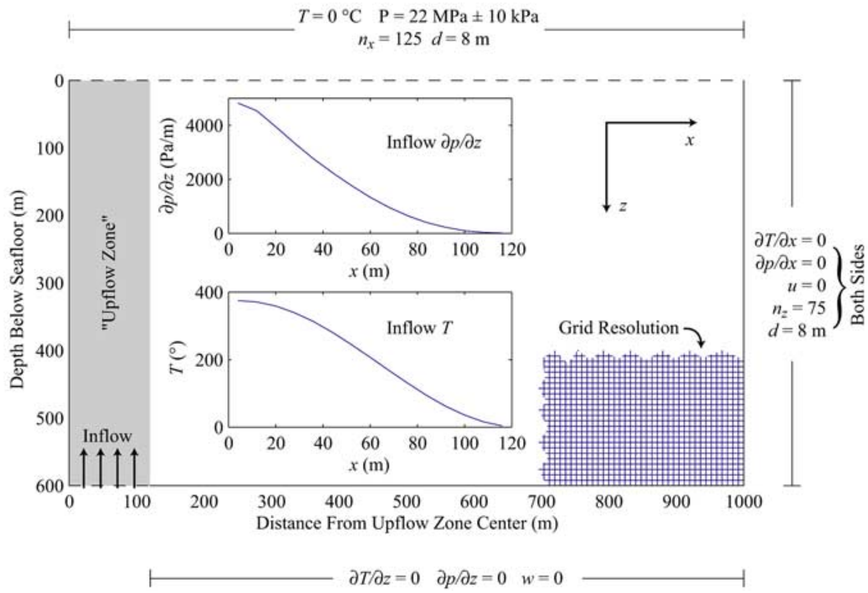

Figure 4. Geometry and boundary conditions for the models presented in this paper. We model a cross section of the crust near a hydrothermal upflow zone from the seafloor to 600 m depth and out to 1000 m from the center of the upflow zone. The upper boundary is open to fluid flow, as is a small section of the bottom boundary where fluid enters the upflow zone. The other boundaries are closed to fluid flow. All boundaries are closed to conductive heat transport, but heat is transported through open boundaries via advection. The inset graphs show the pressure gradient and temperature boundary conditions on the 120-m open section of the bottom boundary. Pressure gradients are cold hydrostatic along this section of the bottom boundary. Displacements are zero on the side and bottom boundaries. Shear stress is zero on all boundaries. We solve the poroelastic convection equations on a 125 × 75 grid, with each grid cell measuring 8 m × 8 m. A sample of the grid resolution is shown in the bottom right-hand corner of the domain. We run models with uniform formation properties, and models with varying permeability and P wave velocity in the upflow zone (Table 3). We also run models in which we simulate a fault zone away from the upflow zone, and we extend the model to incorporate seismic layer 2B/C.

recharge zone, although it is not unreasonable to assume that the geothermal gradient is negligible in the upper 600 m of young oceanic crust in regions of significant downwelling.

[26] Table 3 lists the permeability and P wave velocity in the upflow and recharge zones for Models 1–7. Model 1 is the baseline model and has a uniform permeability (10^{-13} m^2) and P wave velocity (2400 m s^{-1}). We have chosen this permeability such that the diffusive component of pressure perturbations will not interact significantly with the impermeable bottom boundary. All other fluid-independent values take on the layer 2A values in Tables 1 and 2. The temperature and pressure dependent fluid properties are computed using the equation of state described previously. Model 2 has a lower P wave velocity throughout (2000 m s^{-1}), making it more compliant, and Model 3 has a higher P wave velocity throughout (3000 m s^{-1}), making it more stiff. The elastic properties corresponding to these P wave velocities are shown in Table 4. Model 4 has a lower P wave velocity in the upflow zone (2000 m s^{-1}), and Model 5 has a higher P wave velocity in the upflow zone (3000 m s^{-1}). Model 6 has a higher permeability (10^{-12} m^2) in the upflow zone, and Model 7 has a lower permeability (10^{-14} m^2) in the upflow zone.

[27] To obtain a solution, each of these models was first allowed to come to steady state with the pressure at the top of the domain fixed at 22 MPa. This steady state solution provided the reference pressure p_0, corresponding to the zero-strain con-

Table 3. Two-Dimensional Models

	Upflow Zone		Recharge Zone	
Model	k, m^2	V_P, m s^{-1}	k, m^2	V_P, m s^{-1}
1	10^{-13}	2400	10^{-13}	2400
2	10^{-13}	2000	10^{-13}	2000
3	10^{-13}	3000	10^{-13}	3000
4	10^{-13}	2000	10^{-13}	2400
5	10^{-13}	3000	10^{-13}	2400
6	10^{-12}	2400	10^{-13}	2400
7	10^{-14}	2400	10^{-13}	2400

Table 4. Fluid-Independent Elastic Properties

V_P, m s^{-1}	λ, GPa	G, GPa	K, GPa	α
2000	1.03	0.40	1.3	0.97
3000	17.5	0.89	18.1	0.64

dition. Subsequently the periodic tidal loading function was activated, and the model was allowed to complete several tidal cycles in order to let transient signals associated with the initial conditions diminish.

3.4. Two-Dimensional Results and Discussion

[28] Figure 5 shows the steady state flow and temperature solution for Model 1. Shaded contours indicate the temperature field, which ranges from about 0–375°C. Arrows indicate the Darcy velocity field on a logarithmic scale. The hot fluid that is forced in through the open section on the bottom boundary rises through the model domain and exits at the seafloor. This upwelling fluid conductively warms adjacent fluid, driving secondary convection in the remainder of the model domain. Slightly more fluid exits the top boundary than enters the bottom and this is balanced by slow downwelling in the recharge zone.

3.4.1. Predicted Pressure Perturbations

[29] The time-varying pressure condition on the top boundary causes poroelastic pressure fluctuations within the model domain. Figure 6 shows these pressure fluctuations over the course of a single semidiurnal tidal cycle for Model 1. The shaded contours in each panel depict the pressure perturbation at ten times during the 12.5-hour cycle. The tidal stage for each panel is indicated by the red dot on the curve to the upper left of each panel. The panels are spaced 75 min apart in time.

[30] The diffusive component of p' dominates in the upper part of the model. On a rising tide (Figure 6b), a positive pressure perturbation diffuses into the model domain. On a falling tide (Figure 6h), a negative pressure perturbation diffuses into the domain. Near the seafloor the diffusive pressure signal is nearly in phase with the tide, but at greater depths (e.g., at $z \approx 100$ m in Figures 6a and 6f) it clearly lags the tide. As predicted by the one-dimensional model (Figure 3) these diffusive pressure perturbations diffuse deepest at $x \approx 100$ m where the temperatures have intermediate values.

[31] The instantaneous component of p' dominates in the lower part of each model. At high tide (Figure 6c), pressures in the lower part of the domain reach a maximum in response to increased compressive stress at the seafloor. At low tide (Figure 6h), these pressures reach a minimum. In general p' is higher in the recharge zone where fluid is cold and relatively incompressible. In the recharge zone p' is essentially in phase with the tidal loading function, and its value is approximately equal to $\gamma\sigma_B$, as the one-dimensional theory predicts. For Model 1, the loading efficiency in the recharge zone is about 0.5; thus the amplitude of p' is about half the amplitude of the tidal loading

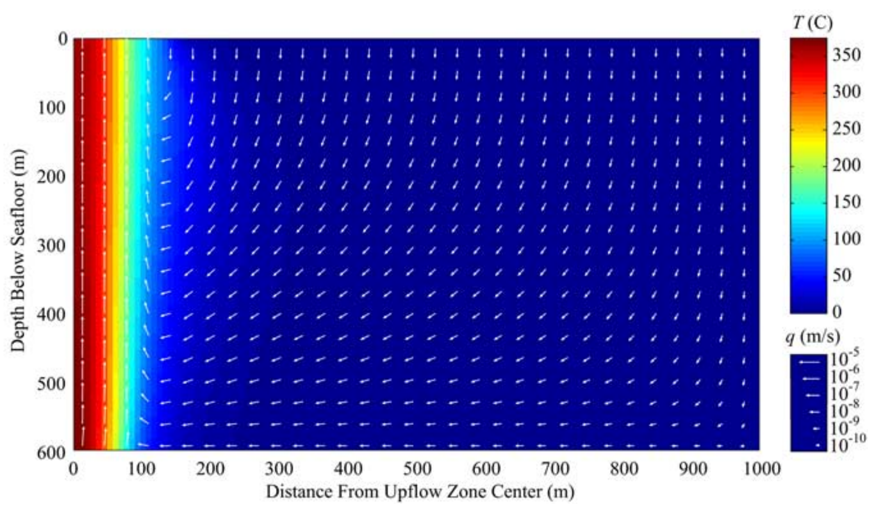

Figure 5. Time-averaged temperature and Darcy velocity field for the baseline Model 1. Shaded contours depict the temperature field; white arrows depict the flow field on a logarithmic scale.

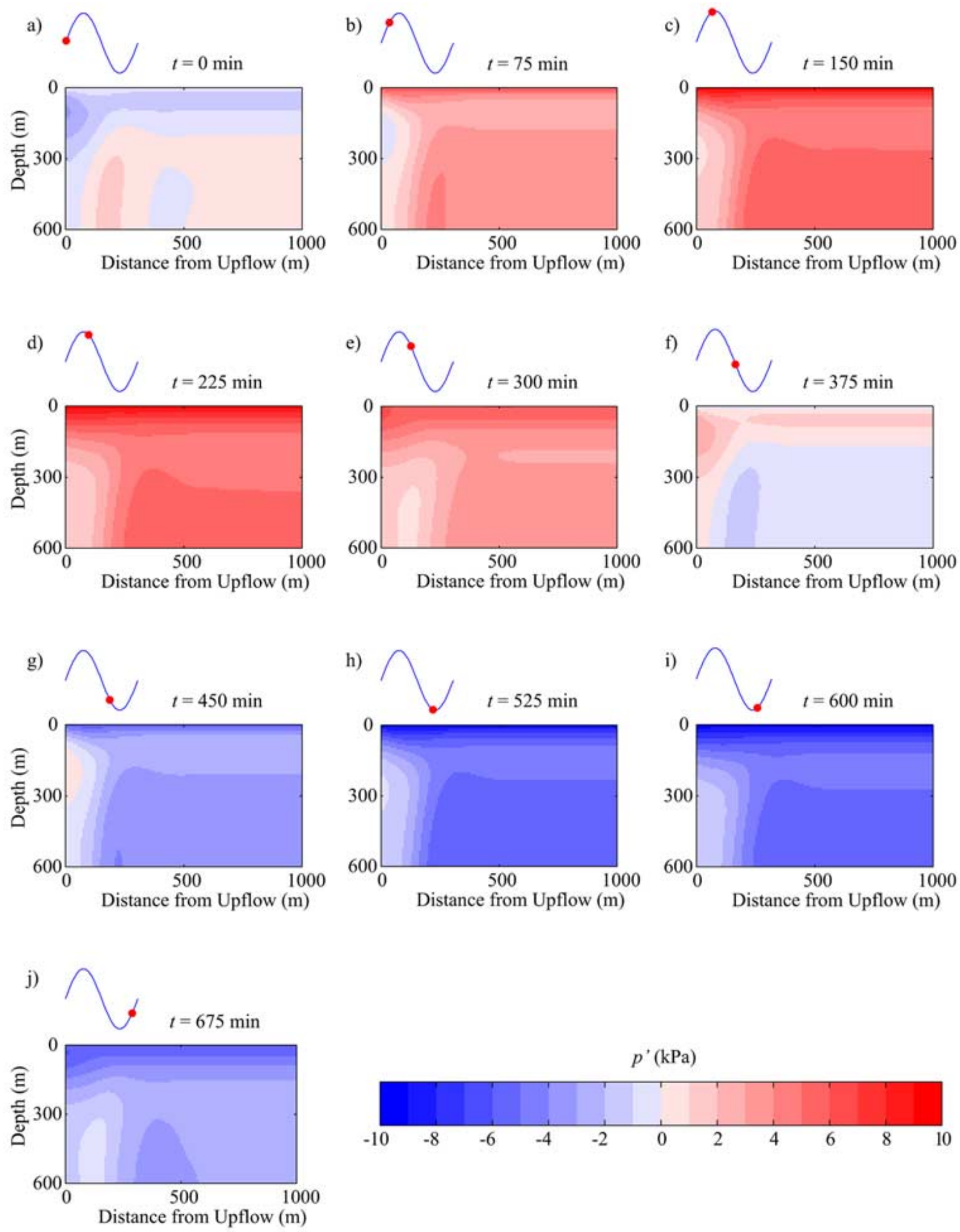

Figure 6. Time-series panels of the pressure perturbation p' over one semidiurnal tidal cycle for Model 1. Shaded contours depict the pressure perturbation within the model as a result of tidal loading, with red and blue colors indicating positive and negative perturbations, respectively. The phase of the tidal loading function is shown by the red dot on the curve in the top left corner of each panel. The time after the start of the tidal cycle (in minutes) is indicated for each panel. The diffusive component of the pressure perturbation dominates in the upper part of the model domain, while the instantaneous component of the pressure perturbation dominates in the lower part of the model domain.

function. Near the upflow zone, where horizontal gradients in the fluid compressibility exist, γ does not accurately predict the pressure perturbation amplitude. This is because horizontal variations in γ lead to pressure gradients that drive flow. At high tide, fluid is forced from higher loading efficiency regions into the upflow zone, raising pressures deep within the model in the upflow zone, and lowering pressures in the adjacent region (e.g., at $z \approx 300$ m in Figure 6e). This fluid flow is what ultimately produces the low pressure region adjacent to the upflow zone deep within the model when the tidal height is near zero (Figure 6f).

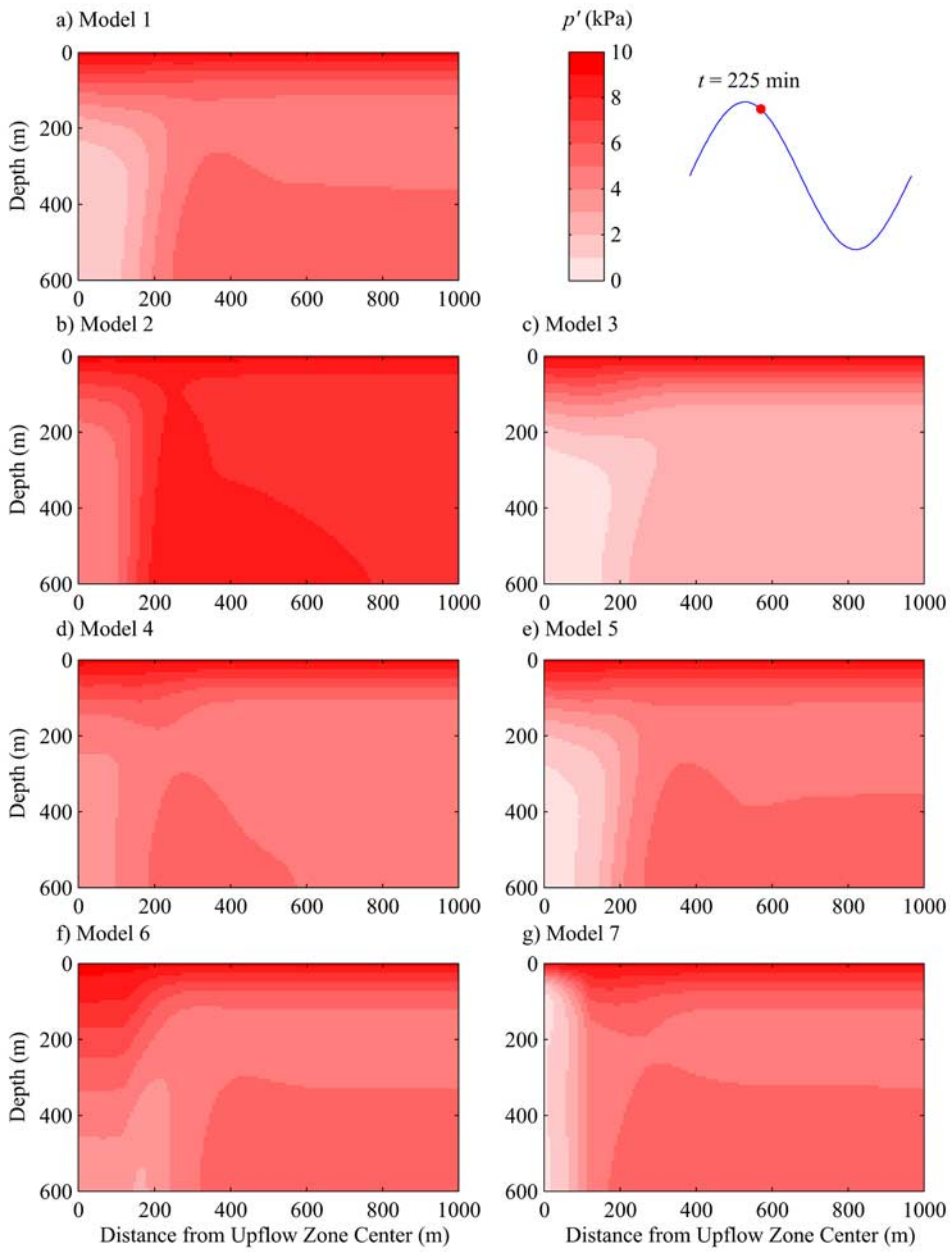

Figure 7. Pressure perturbation p' as a function of depth below the seafloor and distance from the upflow zone center for Models 1–7 (Table 3) just after high tide (t = 225 min). Figure 7a shows the same solution as Figure 6d.

[32] When stiffness and permeability are altered, a slightly different picture emerges. Figure 7 shows the pressure perturbation field for Models 1–7 at a time just after high tide (t = 225 min). For reference, Model 1 is shown in Figure 7a, wherein the p' field is identical to Figure 6d. In Model 2 (Figure 7b), the P wave velocity is reduced to 2000 m s^{-1}, which raises the loading efficiency in the cold part of the model to ~0.8 (compared to ~0.5 for Model 1). Consequently the pressure perturbations are higher at high tide. In the hottest part of this model, the loading efficiency is ~0.2 (compared to ~0.05 for Model 1), but the maximum pressure perturbation in this region is nearly 0.5 times the loading pressure as a result of fluid flow and pressure diffusion from the surrounding high loading efficiency region. In Model 3 (Figure 7c), the P wave velocity is increased to 3000 m s^{-1}, which lowers the loading efficiency in the cold part of the model to ~0.3. Consequently the pressure perturbations are lower at high tide. In the hottest part of this model, the loading efficiency

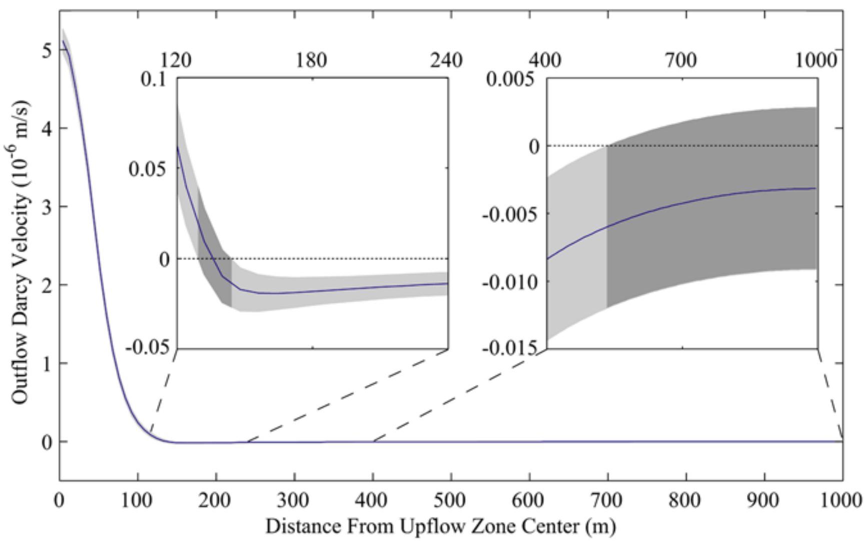

Figure 8. Time-averaged mean Darcy velocity (solid line) and Darcy velocity range (shaded area) at the top of the model domain over a 12.5-hour tidal cycle for Model 1. Inset graphs show these data on expanded y axis scales. Where Darcy velocity reversals occur, the velocity range is shaded with a darker color. In the region where outflow is separated from inflow (near $x \approx 130$), and where outflow is slowest ($x > \sim 500$ m), flow reversals are predicted at the seafloor.

is ~ 0.01, but pressure diffusion from the recharge zone raises p' to ~ 0.06 times the loading pressure. The diffusive component of p' in Models 2 and 3 is similar to Model 1.

[33] In Model 4 (Figure 7d), the P wave velocity is reduced to 2000 m s^{-1} in the upflow zone. This increases the one-dimensional loading efficiency to ~ 0.2 in the hottest part of the upflow zone and to ~ 0.8 in cooler parts of the upflow zone. The loading efficiency in the recharge zone remains at ~ 0.5. The region of very high loading efficiency in the cooler parts of the upflow zone is very narrow, and pressure diffusion prevents the realization of large p' amplitudes in this part of the upflow zone. In Model 5 (Figure 7e), the P wave velocity is increased to 3000 m s^{-1} in the upflow zone. Because loading efficiencies in the upflow zone are already very low in Model 1, increasing the formation stiffness in this part of the model has little effect on p'. The diffusive component of p' and the deep pressure response to tidal loading are also similar to Model 1.

[34] In Model 6 (Figure 7f), the permeability of the upflow zone is increased by a factor of 10, to a value of 10^{-12} m^2. This increases the diffusive length scale in this part of the model by a factor of $\sqrt{10}$, causing the diffusive component of p' to penetrate deeper into the model. The permeability increase in the upflow zone also allows pressure to diffuse more easily into the upflow zone from the surrounding high loading efficiency formation, effectively widening the low p' region deep in the upflow zone. In Model 7 (Figure 7g), the permeability of the upflow zone is reduced by a factor of 10, to a value of 10^{-14} m^2. This reduces the penetration depth of the diffusive component of p' in this region. The permeability decrease in the upflow zone also reduces the ease with which pressure can diffuse from higher loading efficiency regions into the upflow zone, effectively narrowing the low p' region deep in the upflow zone. The p' field deep within Model 7 most closely resembles the predictions of the one-dimensional theory.

3.4.2. Predicted Seafloor Observations of Darcy Velocity

[35] We now consider the effect of these pressure perturbations on the Darcy velocity at the seafloor. Figure 8 shows the time-averaged mean Darcy velocity at the seafloor, which is effectively identical to the steady state Darcy velocity, and the envelope representing perturbations to this flow caused by tidal forcing for Model 1. The results for the other models are similar. The region of mean outflow extends to $x \approx 135$ m with a maximum Darcy velocity of $\sim 5 \times 10^{-6}$ m s^{-1} at $x = 0$ m. Throughout most of this region the tidal perturbations are less than 10% of the outflow velocity. Near the transition from outflow to inflow, where the time-averaged velocities are low, there is a small region extending from $x \approx 130$ m to

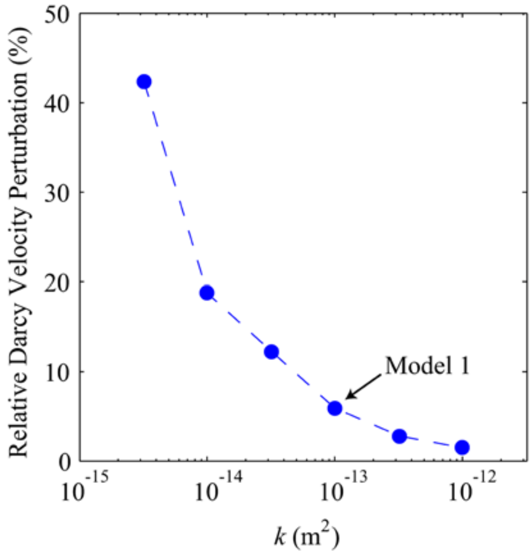

Figure 9. Darcy outflow velocity perturbations relative to the mean Darcy velocity in the highest-temperature fluids for a range of permeabilities. Perturbations in percent are calculated by dividing the range of velocity during a tidal cycle by the mean velocity during the cycle and multiplying by 100. The relative Darcy velocity decreases with increasing permeability.

145 m where flow reversals occur during the tidal cycle. By our definition a flow reversal occurs (both at the seafloor and below it) when the Darcy velocity component in the direction of mean flow changes sign during the tidal cycle. At the top of the recharge zone the inflow velocities are relatively low everywhere, and have a maximum value of $\sim 2 \times 10^{-8}$ m s^{-1}. The tidal perturbations to the mean velocities are significant throughout this region and are sufficient to cause flow reversals at $x > \sim 500$ m.

[36] The relative amplitudes of the tidal perturbations to seafloor outflow and inflow are strongly sensitive to the permeability. Figure 9 shows the relative perturbations in the fastest outflow at $x = 0$ for models with the same parameters as Model 1 except that we consider a range of permeabilities. The perturbations decrease with increasing permeability from 42% at $k = 3.2 \times 10^{-15}$ m^2 to 1.5% at $k = 10^{-12}$ m^2. We stress here that the background Darcy velocity decreases with decreasing permeability faster than the velocity perturbations, so the perturbations increase only in a relative sense.

[37] Figure 10 shows the Darcy velocity phase lag relative to the tidal loading function as a function of position on the seafloor for Models 1–7. For boundary sections where fluid flows out of the domain during any part of the tidal cycle, the phase lag describes the relationship between the time of fastest outflow and the time of high tide. For boundary sections where fluid always flows into the domain, the phase lag describes the relationship between the time of slowest inflow and the time of high tide. In the recharge zone, the Darcy velocity lags the tide by about 135°, as is predicted by the one dimensional modeling of *Jupp and Schultz* [2004]. Near the upflow zone, horizontal gradients in the loading efficiency drive horizontal pressure diffusion near the seafloor, and lead to phase lags

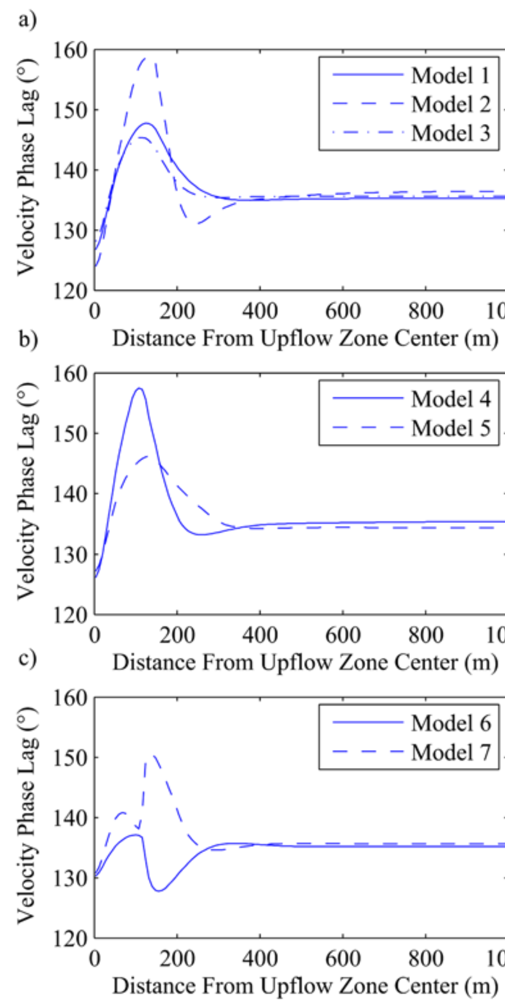

Figure 10. Darcy velocity phase lag relative to the tidal loading along the top boundary for (a) Models 1–3, (b) Models 4–5, and (c) Models 6–7. For locations where fluid flows out of the domain during some or all of the tidal cycle, the lag is the phase of maximum outflow relative to high tide. For locations where fluid always flows into the domain, the lag describes the phase of minimum inflow relative to the high tide.

which diverge from the one-dimensional predictions. In Model 1, the temperature gradient in the upflow zone leads to a gradient in the loading efficiency that drives fluid into the hottest part of the upflow zone at high tide. Fluid flowing into the hottest part of the upflow zone decreases the velocity phase lag at the seafloor. Fluid flowing out of the adjacent region increases the phase lag at $x \approx 120$ m. Models 2–5 show similar phase lag perturbations, but the effect is amplified in Models 2 and 4 because both models are more compliant in the upflow zone, making the loading efficiency a stronger function of temperature (Figure 2), and increasing the loading efficiency gradient. In Models 6 and 7, the differences in permeability between the upflow and recharge zones also influence the phase lag. In Model 6 the permeability is higher in the upflow zone, and as a consequence the penetration depth is greater. Near high tide this leads to pressure gradients that drive flow out of the upflow zone. As a consequence the phase lags decrease in regions adjacent to the upflow zone. The opposite occurs for Model 7.

[38] These results have significant implications for field measurements at mid-ocean ridge hydrothermal systems because they suggest that velocity measurements at or just below the seafloor may provide significant constraints on the underlying structure of mid-ocean ridge hydrothermal systems. Since the predicted relative amplitude of the perturbations decreases with increasing permeability, the tidal perturbations may be largest in regions of low permeability and weak outflow. However, since the permeability structure surrounding black smokers may violate the continuum hypothesis that underlies our models, we cannot exclude the possibility that significant variations in tidal velocity might be observed in vigorous vents with high permeability.

[39] Historically velocity measurements at the seafloor have been very difficult and most measurements have large uncertainties. There are relatively few time-series measurements of outflow, but some studies have reported evidence for tidal perturbations of 2–10% of the mean flow velocity in diffuse systems venting at 10–40°C [e.g., *Jupp*, 2000; *Pruis and Johnson*, 2004; *Schultz et al.*, 1996]. The amplitude of these perturbations are compatible with our models and are consistent with our inference that the largest relative velocity perturbations may be observed in weaker flows. However, higher-quality time series measurements are required before flow observations can be interpreted more extensively with the predictions of poroelastic models.

[40] Flow reversals at the seafloor would also have significant implications for biological communities inhabiting diffuse flow regions where seawater and hydrothermal fluid mix [*Huber et al.*, 2003]. Such flow reversals will bring seawater that contains electron acceptors (e.g., O_2, SO_4^{2-}, NO_3^-) into the shallow crust during part of the tidal cycle, and hydrothermal fluid to the same crustal volumes during the rest of the tidal cycle. It is plausible that subseafloor organisms have developed specific adaptations for this, or that communities of organisms work together to exploit the periodic delivery of hydrothermal energy sources and seawater electron acceptors. *Delaney et al.* [1998] hypothesize that microbes bloom on eruptive timescales with the onset of vigorous fluid flow following a magmatic eruption. Similarly, organisms in the shallow crust may undergo periodic production on tidal timescales with the alternating flow of oxidizing and reduced fluids.

3.4.3. Predicted Seafloor Observations of Temperature

[41] We can also use our models to predict the tidally induced variations in venting temperatures in regions of outflow. In our models, such fluctuations result because the isotherms are advected horizontally by tidally induced flow. The largest temperature fluctuations are observed at the boundary of the upflow zone where the temperature gradients are large. However, even in these regions the largest perturbations in our models are only $\sim 10^{-4}$°C. Figure 11 shows one example for Model 6.

[42] Such small temperature changes would be difficult to detect on the seafloor. Indeed they are less than the adiabatic temperature change that would be created by a 1-m tide ($\sim 10^{-2}$°C for 350°C vent fluids). However, our continuum models may substantially under-predict the temperature change that would be observed in a real system. In equation (27), we make the assumption that all of the wall rock is in complete thermal equilibrium with the fluid. For a fractured medium it is possible that only a small fraction of the rock will remain in thermal equilibrium with the fluid on tidal timescales. For example, in a system of planar cracks with a permeability of 10^{-13} m^2 and crack widths of 0.5 mm, the cracks would be separated by $\sim$100 m. The conductive length scale for periodic heating on a semi-infinite half-space [*Turcotte and Schubert*, 1982] is $\sqrt{\kappa t/\pi}$ where κ is the thermal

Geochemistry Geophysics Geosystems G3

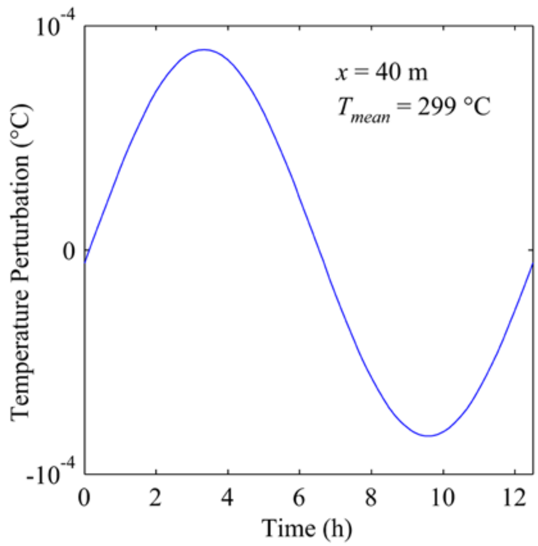

Figure 11. Temperature perturbation time series referenced to the mean temperature of 299°C over one tidal cycle from the top grid-cell row at x = 40 m for Model 6. Perturbations were calculated by integrating the product of the horizontal Darcy velocity and the horizontal temperature gradient with respect to time.

diffusivity of the wall rock. For basalt, κ is about 6.8×10^{-7} m^2 s^{-1}, and with a time t of 12.5 hours, the conductive length scale takes on a value of ~10 cm. Thus only about 0.2% of the rock will be in thermal equilibrium with the fluid when the fluid temperature is maximally perturbed and the temperature perturbation would be amplified by a factor of ~500 relative to our model. For a permeability model described by uniformly spaced tubular cracks with the same permeability and tube diameters of 3 mm, the tubes would be separated by about 4 m and the conductive length scale would be slightly smaller. In this situation only about 0.1% of the wall rock will be in thermal equilibrium with the fluid, and the temperature perturbations predicted by our model could be amplified to ~0.1°C.

[43] Tidal variations in previously collected temperature measurements in both high temperature and diffuse flow [e.g., *Jupp*, 2000; *Larson and Lilley*, 2002; *Pruis and Johnson*, 2004; *Schultz et al.*, 1992, 1996] range from about 0.1°C to 4°C. These values overlap with, but are generally slightly larger than, the maximum temperature perturbations we predict from our continuum models by considering the fraction of wall rock that remains in thermal equilibrium with the fluid on tidal timescales. Thus it seems likely that some of these measurements are affected by processes that are not included in our model.

[44] It is possible to envision pathological cases for a cracked medium in which a change in the direction of horizontal pressure gradients during the tidal cycle would lead to a substantial change in the temperature of fluid in a particular crack. This process is illustrated in Figure 12. In this hypothetical situation, warm fluid flows to the seafloor in one crack, and hotter fluid flows to the seafloor in an adjacent crack. The two cracks are connected near the seafloor by a horizontal crack. When the tidally induced horizontal pressure gradient drives flow to the left, the temperature of the hot fluid in the left-hand crack would be reduced as cooler fluid flows in from the right. The temperature in the right-hand crack would be unaffected during this phase of the tide. When the horizontal pressure gradient drives fluid in the opposite direction, the temperature of the warm fluid in the right-hand crack would be increased as hotter fluid flows in from the left. The temperature in the left-hand crack would be unaffected during this phase of the tide.

3.4.4. Enhanced Dispersion and Fluid Exchange

[45] In a paper discussing off-axis marine hydrothermal systems, *Davis et al.* [2000] suggest that flow perturbations driven by tides may play a role in stimulating microbiological activity below the seafloor through enhanced mixing by hydrodynamic dispersion. This process may have significant implications for the productivity of subseafloor microbial communities because the chemolithotrophic organisms are dependent upon the chemical disequilibrium that results when hot hydrothermal

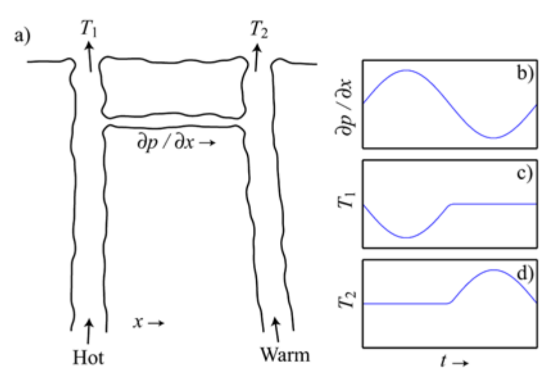

Figure 12. Schematic diagram showing a situation in which tidally induced reversals in the horizontal pressure gradient could result in large temperature perturbations at the seafloor. (a) Crack arrangement; (b) hypothetical time series of the horizontal pressure gradient in the horizontal channel; (c) the temperature measured at T_1; and (d) the temperature at T_2.

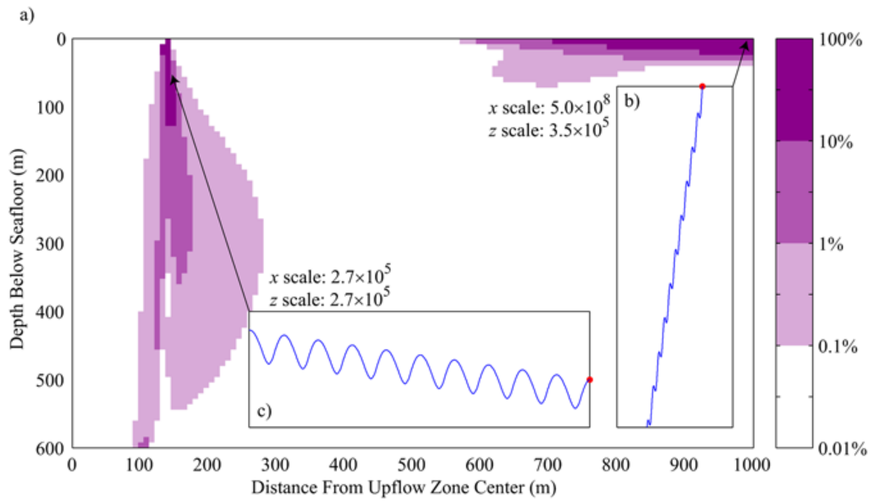

Figure 13. (a) Shaded contours of path length increase on a logarithmic scale, and (b and c) two representative fluid path lines over 10 tidal cycles for Model 1. Path length increase is the percent increase in the length of path line segments due to tidal forcing, such that a 100% increase represents a doubling of the path line segment length. The inset figures show examples of path line segments in two regions where path length increase is significant: (b) in the slow flow near the seafloor on the right-hand side of the model domain and (c) in the zone separating upflow from downflow. The numbers next to the insets show their scaling relative to the main figure. Note that in Figure 13b the x axis is more exaggerated than the z axis to better show the flow reversals.

fluids mix with colder seawater [*McCollom and Shock*, 1997].

[46] Mechanical dispersion is the predominant mechanism for the redistribution of chemical tracers in a mid-ocean ridge hydrothermal system [*Bear*, 1972]. It arises because, on the pore scale, fluid parcels moving within a porous medium do not all have the same velocity as the average flow. The material that makes up the porous medium forces fluid parcels to deviate from the mean flow velocity, as the fluid must flow around particles within the medium. Those parcels of fluid carry any tracers they have with them, resulting in the redistribution of the tracers within the bulk fluid. Mixing occurs when, on the smallest scales, this process brings different water masses in close proximity to one another, and molecular diffusion enables them to exchange their tracers. The dispersivity, a property of the medium controlled by the geometry of the pore space, describes, on average, how pore-scale velocity deviations will redistribute tracer particles for a given average velocity field. Although it is a complex process, the amount of dispersion and dispersive mixing in a given medium is, to a first approximation, dependent on the total distance traveled by a fluid parcel. Tidal forces will enhance dispersive mixing in mid-ocean ridge hydrothermal systems if they increase the distance fluid parcels travel as they traverse the system.

[47] Another possible mechanism for the tidal stimulation of microbiological productivity within mid-ocean ridge hydrothermal systems is enhanced pore-scale fluid exchange. In general, tidal variations in the direction of pressure gradients will cause fluids to flow through different pathways within the porous medium during different tidal phases. This may bring periodic fluid flow to pore space that would be relatively stagnant in the absence of tides. This process could potentially increase the amount of substrate that is exposed to disequilibrium chemical conditions, and thus may have significant implications for subseafloor microbes, especially those hypothesized to inhabit biofilms [*Pysz et al.*, 2004].

[48] Like mechanical dispersion, this process is also complex, and the extent of its effect requires detailed knowledge of the geometry of the porous medium. We assume that enhanced fluid exchange can also be approximated by the increased distance traveled by fluid parcels within the porous medium. This is a good assumption except where increases in flow distance are caused by flow reversals rather than flow deflections.

[49] To explore the possible extent of tidally enhanced mechanical dispersion and fluid exchange, we compute the increase in fluid path length due to tidal forcing as a function of position within the model domain. Figure 13a shows the percentage increase in fluid path length

for Model 1. Throughout most of the model domain, tidal loading leads to negligible changes in path length. Near the seafloor, both the flow and the tidal pressure gradients are near vertical, and wherever the flow speed is relatively fast, the oscillatory pressure gradients are sufficient to change the flow speed but are insufficient to reverse the flow and increase path length. On the right-hand side of the model, where the flow speeds are relatively slow, tidal pressure gradients are sufficient to reverse the flow and significantly increase path length. Figure 13b shows a representative fluid path line segment that has been tidally altered in this way. Oscillatory pressure gradients near the seafloor also lead to significant path length increase within the narrow region separating upflow from downflow at about x = 140 m, where fluid flow is horizontal. Figure 13c shows a representative fluid path line segment that has been tidally altered in this way.

[50] In real systems both the permeability and the elastic properties of the medium are likely to be strongly heterogeneous over a range of scales. One can envision the upper crust as a network of highly permeable and weak cracks or cracked zones separated by strong and relatively impermeable regions. There will also be changes in the elastic and hydrological properties at boundaries separating geological units. As discussed by *Wang et al.* [1999], when the seafloor is subjected to tidal loading, these heterogeneities will lead to pressure gradients that drive flow within the oceanic crust.

[51] Although a continuum formulation is not well suited to model the full effects of such heterogeneities, we consider two simple models to explore the potential effects of heterogeneity within mid-ocean ridge hydrothermal systems. The first model is similar to Model 1, except that a vertical fault zone with an elevated permeability of 10^{-12} m^2 and a reduced P wave velocity of 2000 m s^{-1} extends from the seafloor to the bottom of the domain between x = 400 m and x = 520 m. In the second model we expand the domain to cover a 3000 m × 1800 m region and include a boundary between layer 2A and 2B/C at z = 600 m. The properties of each layer are taken from Tables 1 and 2, except that we assume permeabilities of 10^{-12} m^2 and 10^{-14} m^2 for layers 2A and 2B/C, respectively. The permeability in layer 2A is higher than in Model 1 because we are no longer constrained by the desire to keep the penetration depth less than the thickness of layer 2A.

[52] Figure 14 summarizes the results for the fault zone model. The fault zone significantly modifies the time-averaged patterns of downflow (Figure 14a) with sub-vertical flow in the fault zone and sub-horizontal flow to either side. Both the loading efficiency and the penetration depth are substantially higher in the fault zone, leading to large horizontal pressure gradients in this region (Figure 14b). In comparison to Model 1 (Figure 13a), the presence of a fault zone substantially increases the area in which path length increase is significant (Figure 14c). The path length is increased in regions on either side of the fault zone because a significant component of the tidal pressure gradients are perpendicular to the mean flow. The presence of the fault zone substantially decreases mean downflow velocities on the right-hand side of the model leading to an expanded region in which the tidal velocity perturbations significantly increase the path length due to vertical flow reversals.

[53] Figure 15 summarizes the results for the two-layer model. The width of the upflow zone narrows from ∼400 m in layer 2B/C to ∼50 m in layer 2A due to the higher permeability of layer 2A (Figure 15a). Secondary convection velocities are also much higher in layer 2A. Significant pressure gradients are generated near the two-layer boundary because there is a large decrease in loading efficiency as one moves from layer 2A to 2B/C (Figure 15b) [*Wang and Davis*, 1996]. The path length increase plot (Figure 15c) is dominated by a large region of large path length increase on the right-hand side that extends from the seafloor to the layer boundary at z = 600 m. The higher layer 2A permeability in this model allows higher diffusive pressure gradients to penetrate to the base of the layer leading to a large region of oscillatory flow. In layer 2B/C near the two-layer boundary there is a small region of significant path length increase near the transition from upflow to downflow. However in layer 2A the region of potentially significant path length increase at the boundary of upflow and downflow is poorly resolved because the upflow zone is only two grid cells wide.

[54] Tidal forces are likely to significantly enhance mechanical dispersion and fluid exchange in large portions of the crust near mid-ocean ridge hydrothermal systems. Specifically, wherever

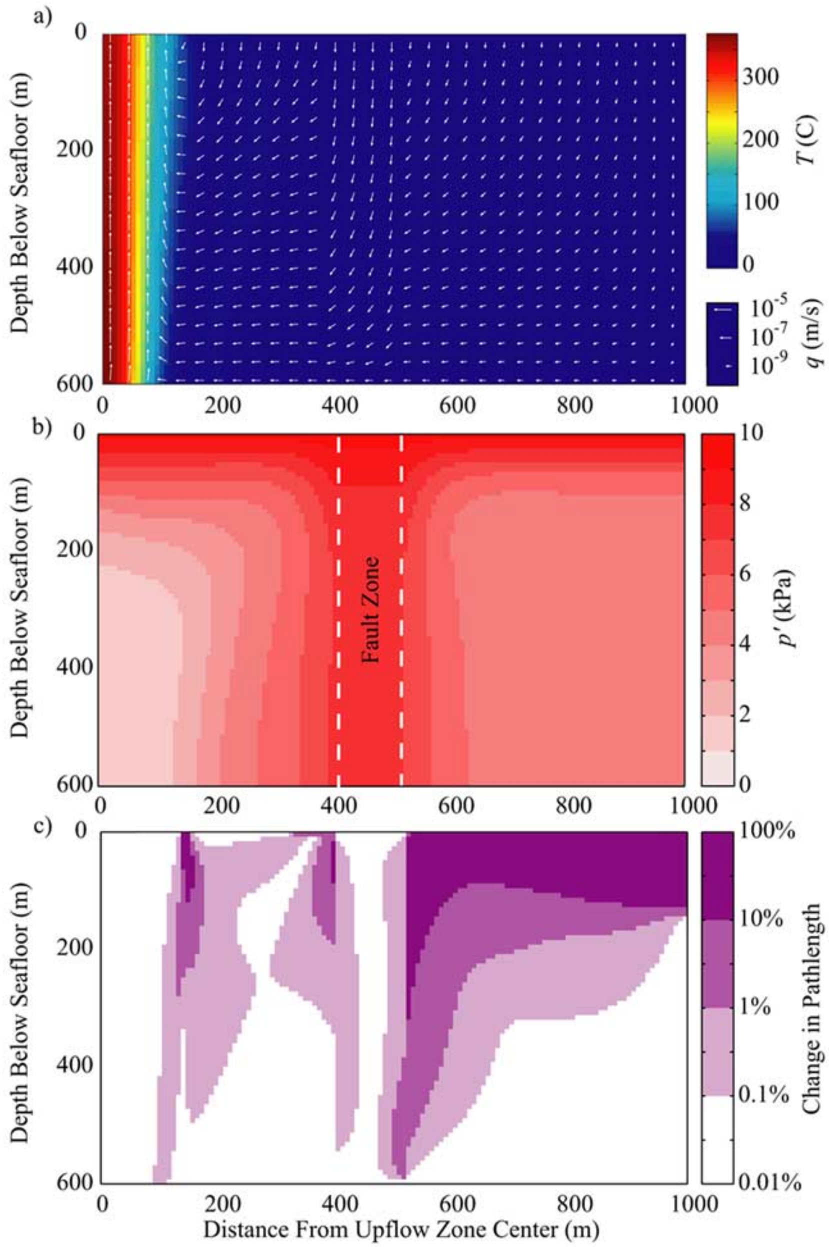

Figure 14. (a) Time-averaged temperature and Darcy velocity field for the fault zone model, plotted using the same conventions as for Figure 5. (b) Pressure perturbation p' for the fault zone model at time $t = 225$ min, plotted using the same conventions as for Figure 7. (c) Shaded contours of path length increase for the fault zone model, plotted using the same conventions as for Figure 13.

flow is relatively slow near the seafloor, flow reversals can increase dispersive mixing within the crust. Also, wherever horizontal flow exists near the seafloor or near a horizontal geological boundary that generates vertical pressure gradient perturbations (such as the boundary between layer 2A and 2B/C), tidal forces may enhance mechanical dispersion and fluid exchange. Increased permeability in layer 2A may expand the region where flow reversals lead to significant mixing. Furthermore, fault zones may generate horizontal pressure gradient perturbations within vertical flow that also lead to mechanical mixing and enhanced fluid exchange. In fact, any heterogeneity in the fluid properties, or the elastic or hydrological properties of the crust will generally tend to enhance mechanical mixing and fluid exchange. And because heterogeneities are

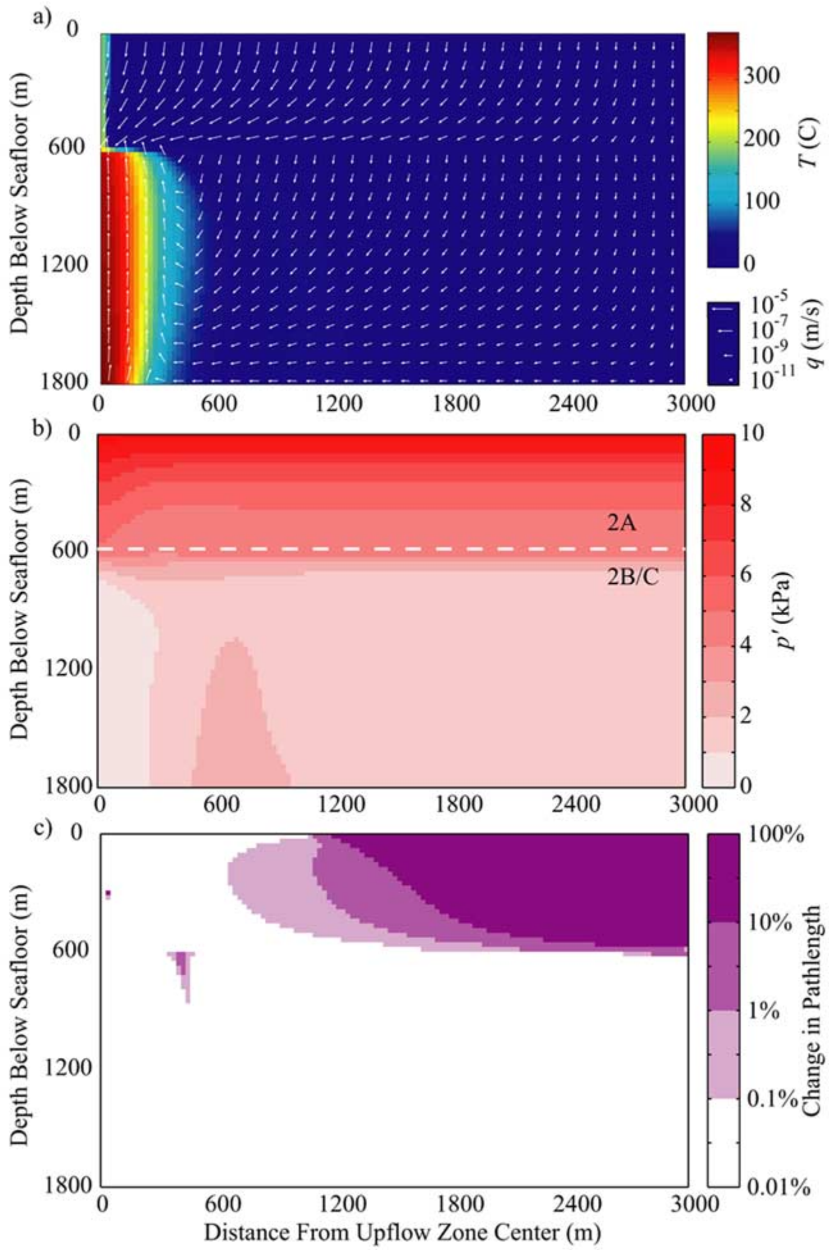

Figure 15. (a) Time-averaged temperature and Darcy velocity field for the two-layer model, plotted using the same conventions as for Figure 5. (b) Pressure perturbation p' for the two-layer model at time t = 225 min, plotted using the same conventions as for Figure 7. (c) Shaded contours of path length increase for the two-layer model, plotted using the same conventions as for Figure 13.

ubiquitous in real mid-ocean ridge hydrothermal systems, tidally enhanced mixing and fluid exchange may be widespread.

4. Conclusion

[55] In this paper, we have explored a one-dimensional analytical model of tidal loading on a poroelastic half-space and a two-dimensional finite-volume model of tidal loading on a poroelastic hydrothermal convection cell in order to explore the effects of ocean tides on mid-ocean ridge hydrothermal systems. The principal conclusions of this study are as follows:

[56] 1. The one-dimensional models show that for a reasonable range of elastic, hydrological and fluid properties, the loading efficiency in young oceanic crust may vary from near zero to near unity

Table A1. Convection Benchmarks

Rayleigh Number	Nusselt Number: This Paper	*Cherkaoui et al.* [1997]	*Ni and Beckermann* [1991]	*Shiralkar et al.* [1983]	*Walker and Homsy* [1978]
100	3.108	3.102	3.103	3.115	3.097
500	8.805	8.880	8.892	8.944	8.66
1000	13.02	13.27	13.42	13.534	12.96

and the diffusive penetration depth may vary from tens of meters to kilometers. The two-dimensional models demonstrate that tides may generate significant vertical and horizontal pressure gradients in mid-ocean ridge hydrothermal systems as a result of spatial variations in fluid temperatures and the elastic and hydrological properties of the crust.

[57] 2. The models suggest that the perturbations in the venting temperature of mid-ocean ridge hydrothermal systems induced by tidal loading are likely to be no more than $\sim$0.1°C and may be much smaller. In many cases, such temperature perturbations would be below detection levels.

[58] 3. On the other hand, the models predict that the fluid velocities at the seafloor may vary substantially with tides. For high-temperature vents the fluctuations in outflow velocity normalized to the mean value increase as the permeability decreases. The velocities in some regions of net low-temperature outflow and net inflow may reverse during the tidal cycle. Such flow reversals may play an important role in mediating biological production just below the seafloor. Also, because flow velocities are predicted to be sensitive to tidal loading, we suggest that new efforts be made to collect high-quality time series measurements of hydrothermal flow in mid-ocean ridge settings.

[59] 4. In the subseafloor, tidally induced velocity perturbations are likely to significantly enhance dispersive mixing and fluid exchange below the seafloor in regions of slow flow and in regions where there are strong gradients in temperature or in the mechanical and hydrological properties of the crust. This process may significantly enhance microbial production in the subseafloor. Models with realistic heterogeneity and explicit cracks will be required to further investigate the physics of this process, and could be combined with thermodynamic models of fluid chemistry to predict the effect of tides on subseafloor microbiological communities.

Appendix A: Numerical Benchmarks

[60] There are no published solutions available to benchmark our entire code, so we evaluated the accuracy of the porous convection and poroelastic components separately. To evaluate the porous convection component, we configured our model so solutions could be compared to previously published solutions for steady convection in a porous layer heated from the side. We computed pressure and temperature solutions on a 50 $\times$ 50 square grid, with all boundaries closed to flow, the top and bottom boundaries adiabatic, and the side boundaries isothermal. We used layer 2A model parameters except for the permeability which was adjusted to give the desired Rayleigh number, defined as

$$Ra = \frac{k\alpha_f \rho_f^2 \mathbf{g} c_f h \Delta T}{\mu \lambda_s}, \quad \text{(A1)}$$

where α_f is the coefficient of fluid thermal expansion, ΔT is the temperature difference across the model domain and h is the height of the model domain. For models with three different Rayleigh numbers, our numerical solutions fall within the range of previously published values (Table A1).

[61] To evaluate the poroelastic component of our code, we first compared isothermal solutions to the one-dimensional analytical solution of *Wang and Davis* [1996]. We set the top boundary open to fluid flow and the model domain depth to approximately three times the predicted penetration depth to prevent the diffusive component of the pressure change from interacting with the impermeable bottom boundary (the analytical solutions are for an infinite half-space). To obtain an initial condition for this test we use an iterative method to compute a hydrostatic pressure condition that converges to

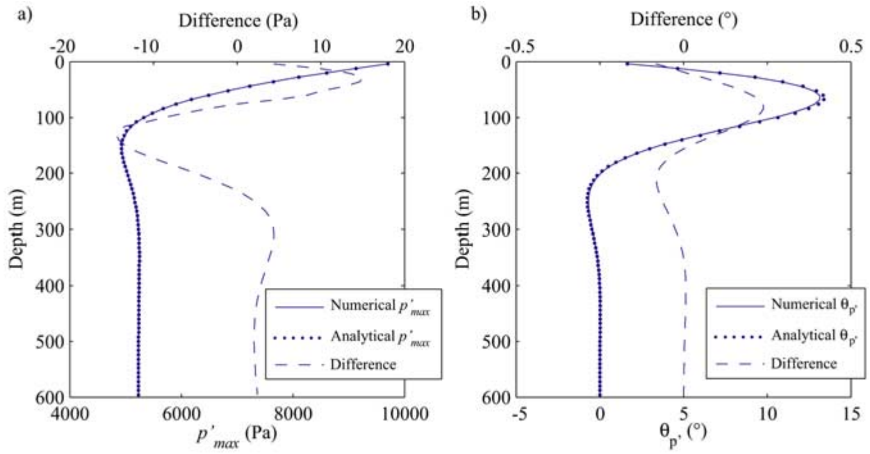

Figure A1. (a) Pressure results and (b) phase lag results of a one-dimensional isothermal benchmark for the poroelastic response to a 1-m-amplitude 12.5-hour tide assuming layer 2A properties (Tables 1 and 2). (a) Maximum pressure perturbation over one 12.5-hour tidal cycle p'_{max} as a function of depth below the seafloor for the analytical (dotted line) and numerical (solid line) models, and the difference between the two models (dashed line). For a tidal loading function amplitude of 10^4 Pa, the difference between the models is less than 20 Pa at all depths, and at many depths the difference is significantly less. (b) Phase lag of the pressure perturbation relative to the 12.5-hour tidal loading function $\theta_{p'}$ as a function of depth below the seafloor for the analytical (dotted line) and numerical (solid line) models, and the difference between the two models (dashed line). At all depths the disagreement between the two models is less than 0.25°, which corresponds to a time of less than 30 s.

zero flow. We then allow the model to complete 20 semidiurnal tidal cycles to let the effects of this initial condition diminish before comparing to the analytical solution. Figure A1 shows the results for a typical comparison. Figure A1a shows the maximum pressure perturbation over one tidal cycle as a function of depth below the seafloor for both the analytical and numerical solutions. At all depths the difference between the models is less than 20 Pa for a 10^4 Pa tidal loading amplitude (i.e., less than 0.2%). Figure A1b shows the phase lag of the pressure perturbation relative to the tidal loading function as a function of depth below the seafloor for both the analytical and numerical solutions. At all depths the difference between the models is less than 0.25°, which for a 12.5-hour tidal cycle is ~30 s.

[62] As a second check on the poroelastic component, we compared our numerical solutions to the analytical results of *Jupp and Schultz* [2004]. The configuration was similar to that used in the one-dimensional benchmark described above. The results of these comparisons are shown in Table A2. The work of *Jupp and Schultz* [2004] provides predictions of the Darcy velocity phase lag relative to the tidal loading function for fluid exiting a hydrothermal system. Under one set of conditions, designated "Regime 1" by *Jupp and Schultz* [2004], the penetration depth is much greater than the depth of an impermeable boundary, and exit fluid velocities are predicted to lag the tidal loading function by 90°. We assigned a large permeability to our model (10^{-8} m^2) to simulate this regime, and obtained a similar result. Under another set of conditions, designated "Regime 2", the penetration depth is much less than the depth of an impermeable boundary, and velocities are predicted to lag the tide by 135°. We assigned smaller permeabilities to our model to simulate this regime and for permeabilities down to about 10^{-15} m^2, we

Table A2. Comparison to *Jupp and Schultz* [2004]

		Numerical	Analytical
k, m^2	d, m	θ_q, °	θ_q, °
		Regime 1	
10^{-8}	8	91.27	90
		Regime 2	
10^{-12}	8	135.80	135
10^{-13}	8	135.80	135
10^{-14}	8	137.85	135
10^{-15}	8	154.59	135
10^{-15}	4	141.18	135
10^{-15}	1	135.87	135

obtained similar results provided that the grid spacing was sufficiently small.

Notation

- B Skempton's coefficient.
- c_f fluid specific heat capacity (J kg^{-1} K^{-1}).
- c_s rock specific heat capacity (J kg^{-1} K^{-1}).
- d grid cell dimension (m).
- D_ζ diffusive penetration depth (m).
- f tidal forcing frequency (s^{-1}).
- $\boldsymbol{g}$ gravitational acceleration (m s^{-2}).
- G shear modulus (GPa).
- h total height of model domain (m).
- k permeability (m^2).
- K drained frame bulk modulus (GPa).
- K_f fluid bulk modulus (GPa).
- K_s rock bulk modulus (GPa).
- K_u undrained frame bulk modulus (GPa).
- l total width of model domain (m).
- n_x number of grid cells in the x direction.
- n_z number of grid cells in the z direction.
- p in situ fluid pressure (Pa).
- p_0 reference pressure (Pa).
- p' fluid pressure change (Pa).
- p'_i instantaneous pressure change (Pa).
- p'_d diffusive pressure change (Pa).
- $p'_{\max}$ max. fluid pressure change per cycle (Pa).
- $\boldsymbol{q}$ Darcy velocity (m s^{-1}).
- Q parameter used in Gassmann's equation (GPa).
- Ra Rayleigh number.
- S uniaxial storage compressibility (Pa^{-1}).
- S_ϵ constrained storage compressibility (Pa^{-1}).
- t time (s).
- T temperature (°C).
- u displacement in the x direction (m).
- V_P P wave velocity (m s^{-1})
- V_S S wave velocity (m s^{-1})
- w displacement in the z direction (m).
- x horizontal coordinate (m).
- z vertical coordinate (m).
- α Biot-Willis parameter
- α_f fluid thermal expansion coefficient (K^{-1}).
- γ loading efficiency.
- $\gamma_{\max}$ maximum loading efficiency.
- η hydraulic diffusivity (m^2 s^{-1}).
- $\theta_{p'}$ pressure change phase lag (°).
- θ_q Darcy velocity phase lag (°).
- κ rock thermal diffusivity (m^2 s^{-1}).
- λ drained Lamé parameter (GPa).
- λ_s bulk thermal conductivity (W m^{-1} K^{-1}).
- μ fluid viscosity (Pa s).
- ν drained Poisson's ratio.
- ν_u undrained Poisson's ratio.
- ρ bulk density (kg m^{-3}).
- ρ_f fluid density (kg m^{-3}).
- ρ_s rock density (kg m^{-3}).
- σ_B tidal loading function (Pa).
- σ_b tidal loading function amplitude (Pa).
- ϕ porosity.
- ψ poroelastic stress coefficient.

Acknowledgments

[63] We thank Russ McDuff for his extensive and invaluable assistance at every stage of this study; John Baross, Julie Huber, and Matthew Schrenk for insightful conversations regarding the biological implications of this work; Hal Mofjeld for advice related to the nature of ocean tides; and Tim Jupp for helpful discussions on poroelasticity. This manuscript benefited greatly from the thorough reviews of Robert Lowell, Kelin Wang, and Associate Editor Magali Billen. Support for this study was provided by the National Science Foundation under grant OCE-9629425.

References

Anderko, A., and K. S. Pitzer (1993), Equation of state representation of phase equilibria and volumetric properties of the system NaCl-H_2O above 573 K, *Geochim. Cosmochim. Acta*, *57*, 1657–1680.

Bear, J. (1972), *Dynamics of Fluids in Porous Media*, Elsevier, New York.

Becker, K. (1985), Large-scale electrical resistivity and bulk porosity of the oceanic crust, Deep Sea Drilling Project Hole 504B, Costa Rica Rift, *Initial Rep. Deep Sea Drill. Proj.*, *83*, 419–427.

Biot, M. A. (1941), General theory of three-dimensional consolidation, *J. Appl. Phys.*, *12*, 155–164.

Carlson, R. L. (1998), Seismic velocities in the uppermost oceanic crust: Age dependence and the fate of layer 2A, *J. Geophys. Res.*, *103*(B4), 7069–7077.

Cherkaoui, A. S. M., W. S. D. Wilcock, and E. T. Baker (1997), Thermal fluxes associated with the 1993 diking event on the CoAxial segment, Juan de Fuca Ridge: A model for the convective cooling of a dike, *J. Geophys. Res.*, *102*(B11), 24,887–24,902.

Chevaldonné, P., D. Desbruyères, and M. L. Haître (1991), Time-series of temperature from three deep-sea hydrothermal vent sites, *Deep Sea Res., Part A*, *38*(11), 1417–1430.

Christensen, N. I., and M. H. Salisbury (1972), Sea floor spreading, progressive alteration of layer 2 basalts, and associated changes in seismic velocities, *Earth Planet. Sci. Lett.*, *15*, 367–375.

Christeson, G. L., G. M. Purdy, and G. J. Fryer (1994), Seismic constraints on shallow crustal emplacement processes at the fast spreading East Pacific Rise, *J. Geophys. Res.*, *99*(B9), 17,957–17,973.

Converse, D. R., H. D. Holland, and J. M. Edmond (1984), Flow rates in the axial hot springs of the East Pacific Rise (21°N): Implications for the heat budget and the formations of massive sulfide deposits, *Earth Planet. Sci. Lett.*, *69*, 159–175.

Copley, J. T. P., P. A. Tyler, C. L. V. Dover, A. Schultz, P. Dickson, S. Singh, and M. Sulanowska (1999), Subannual temporal variation in faunal distributions at the TAG hydrothermal mound (26°N), Mid-Atlantic Ridge, *Mar. Ecol.*, *20*(3–4), 291–306.

Davis, E. E., K. Wang, K. Becker, and R. E. Thomson (2000), Formation-scale hydraulic and mechanical properties of oceanic crust inferred from pore pressure response to periodic seafloor loading, *J. Geophys. Res.*, *105*(B6), 13,423–13,435.

Delaney, J. R., D. S. Kelley, M. D. Lilley, D. A. Butterfield, J. A. Baross, W. S. D. Wilcock, R. W. Embley, and M. Summit (1998), The quantum event of oceanic crustal accretion: Impacts of diking at mid-ocean ridges, *Science*, *281*, 222–230.

Detournay, E., and A. H.-D. Cheng (1993), Fundamentals of poroelasticity, in *Comprehensive Rock Engineering: Principles, Practice and Projects*, vol. 2, edited by J. A. Hudson and C. Fairhurst, pp. 113–171, Elsevier, New York.

Fang, W. W., M. G. Langseth, and P. J. Schultheiss (1993), Analysis and application of in situ pore pressure measurements in marine sediments, *J. Geophys. Res.*, *98*(B5), 7921–7938.

Fisher, A. T. (1998), Permeability within basaltic oceanic crust, *Rev. Geophys.*, *36*(2), 143–182.

Fisher, A. T., K. Fischer, D. Lavoie, M. Langseth, and J. Xu (1994), Geotechnical and hydrogeological properties of sediments from Middle Valley, northern Juan de Fuca Ridge, in *Proc. Ocean Drill. Program, Sci. Results*, *139*, 627–647.

Fujioka, K., K. Kobayashi, K. Kato, M. Aoki, K. Mitsuzawa, M. Kinoshita, and A. Nishizawa (1997), Tide-related variability of TAG hydrothermal activity observed by deep-sea monitoring system and OBSH, *Earth Planet. Sci. Lett.*, *153*(3–4), 239–250.

Gassmann, F. (1951), Über die elastizität poröser medien, *Vierteljahrsschr. Nat. Ges. Zürich*, *96*(1), 1–23.

Holzbecher, E. O. (1998), *Modeling Density-Driven Flow in Porous Media*, Springer, New York.

Huber, J. A., D. A. Butterfield, and J. A. Baross (2003), Bacterial diversity in a subseafloor habitat following a deep-sea volcanic eruption, *FEMS Microbiol. Ecol.*, *43*, 393–409.

Hutnak, M., M. E. Torres, H. P. Johnson, and R. W. Collier (1999), Periodic negative heat flow on southern Hydrate Ridge: Implications for the destabilization of gas hydrate, *Eos Trans. AGU*, *80*(46), Fall Meet. Supl., F482.

Johnson, H. P., M. Hutnak, R. P. Dziak, C. G. Fox, I. Urcuyo, J. P. Cowen, J. Nabelek, and C. Fisher (2000), Earthquake-induced changes in a hydrothermal system on the Juan de Fuca mid-ocean ridge, *Nature*, *407*(6801), 174–177.

Johnson, K. S., J. J. Childress, C. L. Beehler, and C. M. Sakamoto (1994), Biogeochemistry of hydrothermal vent mussel communities: The deep-sea analogue to the intertidal zone, *Deep Sea Res., Part I*, *41*(7), 993–1011.

Jupp, T. E. (2000), Fluid flow processes at mid-ocean ridge hydrothermal systems, Ph.D. thesis, Pembroke Coll., Univ. of Cambridge, Cambridge, UK.

Jupp, T. E., and A. Schultz (2004), A poroelastic model for the tidal modulation of seafloor hydrothermal systems*J. Geophys. Res.*, *109*, B03105, doi:10.1029/2003JB002583.

Kadko, D. (1994), Time-series gamma spectrometry of diffuse flow from the North Cleft segment of the Juan de Fuca Ridge, *Eos Trans. AGU*, *75*(44), Fall Meet. Supl., 307.

Kinoshita, M., O. Matsubayashi, and R. P. V. Herzen (1996), Sub-bottom temperature anomalies detected by long-term temperature monitoring at the TAG hydrothermal mound, *Geophys. Res. Lett.*, *23*(23), 3467–3470.

Kinoshita, M., R. P. V. Herzen, O. Matsubayashi, and K. Fujioka (1998), Erratum to 'Tidally-driven effluent detected by long-term temperature monitoring at the TAG hydrothermal mound, Mid-Atlantic Ridge', *Phys. Earth Planet. Inter.*, *109*, 201–212.

Larson, B. I., and M. D. Lilley (2002), Tidal perturbations of a submarine hydrothermal system, *Eos Trans. AGU*, *83*(4), Ocean Sci. Meet. Suppl., Abstract OS31F-94.

Little, S. A., K. D. Stolzenbach, and F. J. Grassle (1988), Tidal current effects on temperature in diffuse hydrothermal flow: Guaymas Basin, *Geophys. Res. Lett.*, *15*(13), 1491–1494.

Lowell, R. P., and L. N. Germanovich (1994), On the temporal evolution of high-temperature hydrothermal systems at ocean ridge crests, *J. Geophys. Res.*, *99*(B1), 565–575.

Luyendyk, B. P. (1984), On-bottom gravity profile across the East Pacific Rise crest at 21° north, *Geophysics*, *49*(12), 2166–2177.

McCollom, T. M., and E. L. Shock (1997), Geochemical constraints on chemolithoautotrophic metabolism by microorganisms in seafloor hydrothermal systems*Geochim. Cosmochim. Acta*, *61*(20), 4375–4391.

McDuff, R. E., and J. R. Delaney (1995), Periodic variability in fluid temperature at a seafloor hydrothermal vent, *Eos Trans. AGU*, *76*(46), Fall Meet. Supl., F710.

Murphy, W. F., L. M. Schwartz, and B. Hornby (1991), Interpretation physics of V_P and V_S in sedimentary rocks, in *Transactions of the SPWLA Thirty-Second Annual Logging Symposium*, pp. FF1–FF24, Soc. of Prof. Well Log Anal., Houston, Tex.

Ni, J., and C. Beckermann (1991), Natural convection in a vertical enclosure filled with anisotropic porous media, *J. Heat Transfer*, *113*(4), 1033–1037.

Patankar, S. V. (1980), *Numerical Heat Transfer and Fluid Flow*, Taylor and Francis, Philadelphia, Pa.

Pitzer, K. S., J. C. Peiper, and R. H. Busey (1984), Thermodynamic properties of aqueous sodium chloride solutions, *J. Phys. Chem. Ref. Data*, *13*, 1–106.

Pros, Z., J. Vaněk, and K. Klíma (1962), The velocity of elastic waves in diabase and greywacke under pressure up to 4 kilobars, *Stud. Geophys. Geod.*, *6*, 347–367.

Pruis, M. J., and H. P. Johnson (2004), Tapping into the subseafloor: Examining diffuse flow and temperature from an active seamount on the Juan de Fuca Ridge, *Earth Planet. Sci. Lett.*, *217*, 379–388, doi:10.1016/S0012-821X(03)00607-1.

Pysz, M. A., C. I. Montero, S. R. Chhabra, R. M. Kelly, and K. D. Rinker (2004), Significance of polysaccharides in microbial physiology and the ecology of hydrothermal vent environments, in *The Subseafloor Biosphere at Mid-Ocean Ridges*, *Geophys. Monogr. Ser.*, vol. 144, edited by W. S. D. Wilcock et al., pp. 213–226, AGU, Washington, D. C.

Sato, T., J. Kasahara, and K. Fujioka (1995), Observation of pressure change associated with hydrothermal upwelling at a seamount in the south Mariana Trough using an ocean bottom seismometer, *Geophys. Res. Lett.*, *22*(11), 1325–1328.

Schultz, A., J. R. Delaney, and R. E. McDuff (1992), On the partitioning of heat flux between diffuse and point source seafloor venting, *J. Geophys. Res.*, *97*(B9), 12,299–12,314.

Schultz, A., P. Dickson, and H. Elderfield (1996), Temporal variations in diffuse hydrothermal flow at TAG, *Geophys. Res. Lett.*, *23*(23), 3471–3474.

Shaw, P. R. (1994), Age variations of oceanic crust poisson's ratio: Inversion and a porosity evolution model, *J. Geophys. Res.*, *99*(B2), 3057–3066.

Shiralkar, G. S., M. Haajizadeh, and C. L. Tien (1983), Numerical study of high Rayleigh number convection in a vertical porous enclosure, *Numer. Heat Transfer*, *6*(2), 223–234.

Tivey, M. K., A. M. Bradley, T. M. Joyce, and D. Kadko (2002), Insights into tide-related variability at seafloor hydrothermal vents from time-series temperature measurements, *Earth Planet. Sci. Lett.*, *202*, 693–707.

Touloukian, Y. S., W. R. Judd, and R. F. Roy (Eds.) (1981), *Physical Properties of Rocks and Minerals*, *McGraw-Hill/CINDAS Data Ser. Mater. Prop.*, vol. II-2, McGraw-Hill, New York.

Turcotte, D. L., and G. Schubert (1982), *Geodynamics: Applications of Continuum Physics to Geological Problems*, John Wiley, Hoboken, N. J.

van der Kamp, G., and J. E. Gale (1983), Theory of Earth tide and barometric effects in porous formations with compressible grains, *Water Resour. Res.*, *19*(2), 538–544.

Vera, E. E., J. C. Mutter, P. Buhl, J. A. Orcutt, A. J. Harding, M. E. Kappus, R. S. Detrick, and T. M. Brocher (1990), The structure of 0- to 0.2-m.y.-old oceanic crust at 9°N on the East Pacific Rise from expanded spread profiles, *J. Geophys. Res.*, *95*(B10), 15,529–15,556.

Walker, K. L., and G. M. Homsy (1978), Convection in a porous cavity, *J. Fluid Mech.*, *87*(Part 3), 449–474.

Wang, H. F. (2000), *Theory of Linear Poroelasticity With Applications to Geomechanics and Hydrogeology*, Princeton Univ. Press, Princeton, N. J.

Wang, K., and E. E. Davis (1996), Theory for the propagation of tidally induced pore pressure variations in layered subseafloor formations, *J. Geophys. Res.*, *101*(B5), 11,483–11,495.

Wang, K., G. van der Kamp, and E. E. Davis (1999), Limits of tidal energy dissipation by fluid flow in subsea formations, *Geophys. J. Int.*, *139*(3), 763–768.

Wilcock, W. S. D., and A. T. Fisher (2004), Geophysical constraints on the sub-seafloor environment near mid-ocean ridges, in *The Subseafloor Biosphere at Mid-Ocean Ridges*, *Geophys. Monogr. Ser.*, vol. 144, edited by W. S. D. Wilcock et al., pp. 51–74, AGU, Washington, D. C.

Wilcock, W. S. D., and A. McNabb (1996), Estimates of crustal permeability on the Endeavour segment of the Juan de Fuca mid-ocean ridge, *Earth Planet. Sci. Lett.*, *138*(1–4), 83–91.